LIMNOLOGY and OCEANOGRAPHY

Predicting effects of ocean warming, acidification, and water quality on Chesapeake region eelgrass

Richard C. Zimmerman,*1 Victoria J. Hill,1 Charles L. Gallegos2

¹Department of Ocean, Earth & Atmospheric Sciences, Old Dominion University, Norfolk, Virginia ²Smithsonian Environmental Research Center, Edgewater, Maryland

Abstract

Although environmental requirements of seagrasses have been studied for years, reliable metrics for predicting their response to current or future conditions remain elusive. Eelgrass (Zostera marina L.) populations of the Chesapeake region lie near the southern limit of their range in the Western North Atlantic, exposing them to increasing thermal stress as the climate warms. However, CO2 stimulated photosynthesis may offset some of the negative effects of temperature stress. The combined effects of temperature, CO₂, and light availability controlled by water quality and epiphytes were explored using GrassLight, a bio-optical model that provided a predictive environment for evaluating the interaction of multiple stressors on eelgrass distribution and density across the submarine landscape. Model predictions were validated against in situ measures of spectral diffuse attenuation, eelgrass density, and distribution. The potential for photosynthesis stimulated by ocean acidification to mitigate the effects of high temperature on eelgrass populations growing near the southern limit of their distribution was explored. The model accurately reproduced the submarine light environment from measured water quality parameters, and predicted their impacts on eelgrass distribution. It also reproduced the negative effects of warm summer temperatures on eelgrass distributions, and demonstrated that CO₂ increases projected for the next century should stimulate photosynthesis sufficiently to offset the negative effects of thermal stress on eelgrass growing in the Chesapeake region, even in the presence of epiphytes. Thus, improved water quality should facilitate the survival of eelgrass populations in Chesapeake region, even in the face of a warming climate.

Seagrass communities are in global decline from environmental change resulting from eutrophication, climate warming, mechanical disturbance, and loss of trophic diversity (Orth et al. 2006b; Hughes et al. 2013). Among these factors, seagrass density and distribution are particularly vulnerable to deteriorating water column transparency resulting from nutrient-stimulated algal growth and sediment loading (Duarte 1991; Nielsen et al. 2002). However, reliable metrics for predicting seagrass distributions from standard water quality measures remain elusive, even to the point of suggesting discontinuous responses to light availability in turbid vs. clear water (Duarte et al. 2007).

The eelgrass (*Zostera marina* L.) communities of the Chesapeake Bay and coastal lagoons of the DelMarVa Peninsula, U.S.A., have been decimated by a series of natural stressors (disease, temperature) and anthropogenic deterioration of water quality since the 1930s that continue to this day (Orth et al. 2006a). Eelgrass has returned to portions of the Chesapeake region characterized by relatively good water quality, particularly along the eastern shore of Chesapeake Bay and

in the southern coastal bays of the DelMarVa Peninsula (Orth et al. 2006a). However, many previously vegetated areas have never recovered, and current bay-wide targets call for restoring submerged aquatic vegetation (SAV) to the 1 m isobath, which is at least 2 m shallower than the historic distribution of SAV in the Chesapeake Bay (Batiuk et al. 1992). Populations in Chincoteague Bay increased steadily from the mid-1980s to about 1999 but have remained stable since then (Wazniak et al. 2007). Eelgrass restoration has been less successful on the western shores of the coastal bays and has succeeded only tenuously in bays near urban centers (Isle of Wight, Assawoman Bay), as well as on the western shore of Chesapeake Bay where water quality is relatively poor. The failures of restoration in most locations, coupled with the recovery plateau in Chincoteague Bay, could be a signal that SAV is poised to decline in the future (Wazniak et al. 2007).

In addition to water quality, temperature has long been known to affect eelgrass abundance and productivity, especially in the Chesapeake region, and climate warming may further stress light-limited populations (Moore and Jarvis 2008). Eelgrass grows well between 10°C and 25°C, but

^{*}Correspondence: rzimmerm@odu.edu

temperatures above 25°C represent stressful conditions for eelgrass growth and temperatures near 30°C could exceed the capacity for acclimation, resulting in eelgrass decline (Thayer et al. 1975; Evans et al. 1986; Zimmerman et al. 1989).

Projecting the response of marine ecosystems to future climate change requires consideration of the simultaneous impacts of multiple factors that can have positive and negative effects on the performance and distribution of key species. Although the high light requirements of seagrasses have often been attributed to respiratory demand of nonphotosynthetic roots and rhizomes (Nielsen et al. 2002), CO₂-limitation of leaf photosynthesis contributes substantially to these high light requirements (Beer and Koch 1996; Zimmerman et al. 1997; Invers et al. 2001). Consequently, elevated concentrations of dissolved inorganic carbon (DIC) in seawater resulting from anthropogenic increase in atmospheric CO₂ concentration may offset some of the negative impacts of climate change on seagrass ecosystems (Palacios and Zimmerman 2007). Although commonly referred to as "ocean acidification" (OA) because it reduces seawater pH and carbonate saturation state (Fabry et al. 2008), the process may be viewed more broadly as "ocean carbonation" (OC) because it also increases the concentration of dissolved aqueous CO₂ [CO_{2(aq)}], a direct substrate for marine photosynthesis.

This study explored the combined impacts of water quality, temperature, and CO2 availability on the density and depth distribution of eelgrass in the Chesapeake region using a biooptical model of water quality impacts on submarine light distribution (Gallegos 1994, 2001) combined with a vertically resolved model of canopy photosynthesis and whole plant carbon balance (Zimmerman 2003b, 2006) that we call GrassLight (Ver. 2.11). This integrated tool provided mechanistically based predictors of submarine spectral irradiance and spectral diffuse attenuation from routine water quality measurements, and determined seagrass canopy photosynthesis, shoot abundance, and distribution across the submarine landscape for specified climates (temperature & CO2 in this case). Our objectives were to (i) validate model predictions against in situ measures of spectral diffuse attenuation, as well as eelgrass density and distribution in the Chesapeake region and (ii) explore the potential for photosynthesis stimulated by OA/OC to mitigate the negative impacts of high summer water temperature on eelgrass populations growing near the southern limit of their distribution in the temperate North Atlantic.

Theoretical development

Modeling the distribution of downwelling spectral irradiance from water quality measures

The *GrassLight* model developed here represents a merger of radiative transfer efforts to establish water quality criteria for seagrass survival (Gallegos 2001), with a vertically resolved model that accounts for the effects of canopy architecture (height, density, leaf orientation, and optical properties) on photosynthetic light absorption and whole-plant

carbon balance (Zimmerman 2003b, 2006). A list of model symbols, their definitions and dimensions are provided in Table 1. The parenthetic notations λ , z, and t indicate wavelength (λ), depth (z), and/or temporal (t) dependence of particular quantities. A solar irradiance model for cloudless atmospheres (Gregg and Carder 1990) was used to compute the downwelling spectral irradiance just beneath the sea surface [$E_{\rm d}(\lambda,0^-)$] at local solar noon as a function of date and location (Latitude, Longitude). Irradiances at depths equivalent to the top of the seagrass canopy [$E_{\rm d}(\lambda,z_{\rm can})$] were determined from $E_{\rm d}(\lambda,0^-)$ according to the Lambert–Beer law:

$$E_{\rm d}(\lambda, z_{\rm can}) = E_{\rm d}(\lambda, 0^{-}) \cdot \exp[-K_{\rm d}(\lambda) \cdot z_{\rm can}] \tag{1}$$

Spectral diffuse attenuation coefficients for downwelling plane irradiance $[K_d(\lambda)]$ were calculated from water column inherent optical properties (IOPs) using the following relationship developed by (Lee et al. 2005; Lee et al. 2007) using extensive simulations with the mechanistic radiative transfer model Hydrolight (Mobley 1989):

$$K_{\rm d}(\lambda) = (1 + 0.005\theta_0) \cdot a_{\rm t}(\lambda) + 4.18 \cdot [1 - 0.52 \cdot \exp(-10.8 \cdot a_{\rm t})] \cdot b_{\rm b}(\lambda)$$
(2)

where θ_0 was the above-water solar zenith angle (degrees). The wavelength-dependent IOPs were the total absorption coefficient $[a_{\rm t}(\lambda),]$ and the backscattering coefficient $[b_{\rm b}(\lambda),]$, both dimensionalized as m⁻¹. Total absorption $[a_{\rm t}(\lambda)]$ is defined as the absorption spectrum for pure water $[a_{\rm w}(\lambda),$ (Pope and Fry 1997)] plus all other dissolved and particulate absorbing components. The non-water absorption coefficient $[a_{\rm t-w}(\lambda)]$ was partitioned into contributions from the following dissolved and suspended constituents:

$$a_{t-w}(\lambda) = a_{g}(\lambda) + a_{\phi}(\lambda) + a_{p-\phi}(\lambda)$$
(3)

where $a_{\rm g}(\lambda)$, $a_{\rm \phi}(\lambda)$, $a_{\rm p-\phi}(\lambda)$ were the spectral absorption coefficients due to colored dissolved organic matter (CDOM), phytoplankton, and non-algal particulates (NAP = sediment and detritus), respectively. The water column IOPs were calculated from concentrations of water quality constituents using mass-specific absorption and scattering coefficients (Gallegos 2001; Biber et al. 2008), with the exception of $a_{\rm g}(\lambda)$, which was represented as a negative exponential function scaled by the absorption at 440 nm (Bricaud et al. 1981; Roesler et al. 1989):

$$a_{g}(\lambda) = a_{g}(440) \cdot \exp\left[-s_{g}(\lambda - 440)\right] \tag{4}$$

The exponential term s_g provided the spectral slope for absorption by CDOM and was set to 0.0184 for all

Table 1. List of model symbols, their definitions and dimensions. Parenthetic notation of λ and z indicates that the quantity is wavelength (λ) and/or depth (z) dependent.

Symbol	Definition	Dimensions
Fundamental quant	ities	
θ_{O}	Solar zenith angle, above water	degrees
Z	Water depth	m
Δz	Vertical thickness of canopy layers	m
[Chl <i>a</i>]	Phytoplankton pigment concentration	${\rm mg~m^{-3}}$
[TSM]	Total suspended matter concentration	$\mathrm{g}\;\mathrm{m}^{-3}$
Radiometric quantit	ties	
$E_{\rm d}(\lambda,z)$	Downwelling spectral plane irradiance at depth z	$\mathrm{W}~\mathrm{m}^{-2}~\mathrm{nm}^{-1}$
		Or
$E_{\rm u}(\lambda,z)$	Upwelling plane irradiance transmitted through layer z	quanta $m^{-2} s^{-1} nm^{-1}$
Vater column inher	rent optical properties (IOPs)	
$a_{\rm t}(\lambda)$	Total absorption coefficient	m^{-1}
$a_w(\lambda)$	Absorption coefficient for pure water	m^{-1}
$a_{t-w}(\lambda)$	Non-water absorption coefficient	m^{-1}
$a_{\rm g}(\lambda)$	CDOM (or gilvin) absorption coefficient	m^{-1}
$a_{\phi}(\lambda)$	Phytoplankton absorption coefficient	m^{-1}
$a_{\mathbf{p}-\phi}(\lambda)$	Non-algal particulate (NAP) absorption coefficient	m^{-1}
$a_{\phi}^{*}(\lambda)$	Chl-specific phytoplankton absorption, or optical cross-section	$m^2 mg^{-1} Chl a$
$a_{p\text{-}\phi}^{\star}(\lambda)$	Mass-specific NAP absorption coefficient, or optical cross section	$m^2 g^{-1} DW$
$b_{ m bp}(\lambda)$	Particulate backscattering coefficient	m^{-1}
$b_{\rm p}(\lambda)$	Particulate scattering coefficient	m^{-1}
$b_{\rm p}^*(\lambda)$	Mass-specific particulate scattering coefficient, or optical cross section	${\rm m}^{-2}~{\rm g}^{-1}~{\rm DW}$
•	for water column inherent optical properties (IOPs)	-
c ₁ , c ₂	Scaling coefficients for $a_{\mathbf{p}-\phi}^{\star}(\lambda)$	$\mathrm{m^2~g^{-1}}$
$S_{\mathbf{g}}$	Spectral slope for $a_q(\lambda)$	Dimensionless
S _{NAP}	Spectral slope for $a_{p-\phi}(\lambda)$	Dimensionless
v_{sa}	Nonlinearity coefficient for $a_{p-\phi}(\lambda)$	Dimensionless
$v_{oldsymbol{\phi}}$	Nonlinearity coefficient for $a_{\phi}(\lambda)$	Dimensionless
υ _{sb}	Nonlinearity coefficient for $b_p(\lambda)$	Dimensionless
η	Spectral exponent for $b_p(\lambda)$	Dimensionless
	rent optical properties (AOPs)	
$K_{\rm d}(\lambda)$	Water column attenuation of downwelling irradiance	m^{-1}
$K_{\rm u}(\lambda)$	Water column attenuation of upwelling irradiance	m^{-1}
$\bar{\mu}_{d}(z)$	Average cosine of downwelling irradiance	Dimensionless
$\bar{\mu}_{u}(z)$	Average cosine of upwelling irradiance	Dimensionless
Submerged canopy		
$a_{L}(\lambda)$	Leaf absorption coefficient	m ⁻¹ of leaf thickness
$a_{\rm epi}(\lambda)$	Leaf epiphytes absorption coefficient	m^{-1} of leaf thickness
$A_{L}(\lambda)$	Photosynthetic leaf absorptance	Dimensionless
β	Nadir bending angle of the submerged plant canopy	Degrees or radians
$A_{\rm epi}(\lambda)$	Leaf epiphyte absorptance	Dimensionless
L_{pred}	Predicted leaf area index of the plant canopy for $P:R=1$	m ² leaf m ⁻² seabed
$I_{p}(Z)$	Horizontally projected leaf area at depth z	m ² leaf m ⁻² seabed
$\rho_{L}(\lambda)$	Leaf reflectance	Dimensionless
$\rho_{d}(\lambda, z)$	Canopy reflectance of downwelling irradiance	Dimensionless
$\rho_{\rm d}(\lambda, z)$ $\rho_{\rm u}(\lambda, z)$	Canopy reflectance of upwelling irradiance	Dimensionless
$\rho_{\rm u}(\lambda, z)$ $t_{\rm L}$	Leaf thickness	m

TABLE 1. Continued

Symbol	Definition	Dimensions
Photosynthetic quantitie	es ·	
PUR(z)	Photosynthetically utilized irradiance in layer z	Mol photons m ⁻² leaf s ⁻¹
ϕ_{p}	Quantum efficiency of photosynthesis	Mol C mol ⁻¹ photons absorbed
P _E	Light-saturated photosynthesis	Mol C m^{-2} leaf s^{-1}
P(z)	Light-dependent photosynthesis at depth (z)	Mol C m^{-2} leaf s^{-1}
$P_{\rm c}(t)$	Instantaneous whole canopy photosynthesis = $\sum P(z)$	Mol C m^{-2} leaf s^{-1}
P_d	Daily integrated canopy photosynthesis = $\sum P_c^z(t)$	$Mol C m^{-2} leaf day^{-1}$
R _{Leaf} , R _{Root} , R _{Rhizome}	Respiration rates of leaf, root and rhizome $\frac{2}{t}$	$Mol C m^{-2} leaf day^{-1}$

simulations (Tzortziou et al. 2006). Absorption by NAP was the product of a mass-specific-absorption spectrum or optical cross section $[a^*_{p-\phi}(\lambda)]$ multiplied by a measure of the concentration of NAP, which we take to be the total suspended matter (TSM):

$$a_{\mathbf{p}-\phi}^*(\lambda) = c_1 + c_2 \cdot \exp[-s_{\text{NAP}}(\lambda - 440)]$$
 (5)

$$a_{p-\phi}(440) = a_{p-\phi}^*(440) \cdot [TSM]^{v_{sa}}$$
 (6)

where c_1 allowed for some small amount of absorption at long wavelengths (typically \leq 2% of value at 440 nm, (Bowers and Binding 2006), c_2 scaled the NAP absorption cross-section at 440 nm, $s_{\rm NAP}$ was the spectral slope of the NAP absorption cross-section, and $v_{\rm sa}$ allowed for nonlinearity in the relationship with TSM. The chlorophyll specific-absorption spectrum, $a_{\phi}^{\star}(\lambda)$, was determined by regression of measured phytoplankton absorption against [Chl a] for various sites around Chesapeake Bay (Gallegos and Neale 2002; Magnusen et al. 2004):

$$a_{\phi}(\lambda) = a_{\phi}^{*}(\lambda) \cdot \left[\operatorname{Chl} a \right]^{v_{\phi}} \tag{7}$$

where the exponent, (v_{ϕ}) controlled the degree of nonlinearity for the relationship between [Chl a] and $a_{\phi}(\lambda)$ (Bricaud et al. 1995), although v_{ϕ} was set to 1 for these simulations.

The particulate scattering spectrum, $b_{\rm p}(\lambda)$, was modeled as a power function of wavelength centered at 555 nm (Snyder et al. 2008):

$$b_{\rm p}(\lambda) = b_{\rm p}(555) \cdot \left(\frac{555}{\lambda}\right)^{\eta} \tag{8}$$

where η represented the nonlinear spectral exponent, and was set to 0.5 for these simulations (Snyder et al. 2008). As with absorption by NAP, the magnitude of scattering at the reference wavelength (555 nm) was scaled by:

$$b_{\rm p}(555) = b_{\rm p}^*(555) \cdot [{\rm TSM}]^{v_{\rm sb}}$$
 (9)

where $b_{\rm p}^*$ (555) was the optical cross-section for backscattering at 555 nm and the exponent ($v_{\rm sb}$) allowed for nonlinearity.

Particulate backscattering ($b_{\rm bp}$) was calculated by multiplying the particulate scattering coefficient by the backscattering ratio ($b_{\rm bp}/b_{\rm p}$), the value of which can be site-specific depending on the composition of the suspended particles (e.g., mineral sediment vs. phytoplankton vs. organic detritus):

$$b_{\rm bp}(\lambda) = b_{\rm p}(\lambda) \cdot \frac{b_{\rm bp}(555)}{b_{\rm p}(555)}$$
 (10)

Although there is no basis for generalizing the spectral shape of the backscattering ratio, errors in calculated $K_{\rm d}(\lambda)$ resulting from spectral variability in $b_{\rm bp}/b_{\rm p}$ can be minimized by scaling the overall magnitude of the ratio near the center (e.g., 555 nm) of the visible spectrum (Snyder et al. 2008).

Modeling marine spectral irradiance through the submerged plant canopy

A two-flow approach was used to propagate $E_{\rm d}(\lambda,z)$ downward through the seagrass canopy and to compute the amount of light absorbed for leaf photosynthesis (Zimmerman 2003b):

$$\begin{split} E_{\rm d}(\lambda,z-1) &= E_{\rm d}(\lambda,z) \cdot [1-\rho_{\rm d}(\lambda,z)] \\ &\quad \cdot \exp\left[-\left\{a_{\rm L}(\lambda) + a_{\rm epi}(\lambda)\right\} \cdot t_{\rm L} \cdot \frac{l_{\rm p}(z)}{\overline{\mu}_{\rm d}(z)} - K_{\rm d}(\lambda,z) \cdot \Delta z\right] \end{split} \tag{11}$$

where $E_{\rm d}(\lambda,z-1)$ represented the spectral downwelling plane irradiance emerging from the layer at z. The term $[1-\rho_{\rm d}(\lambda,z)]$ accounted for the loss of downwelling spectral irradiance by upward reflection at z, which depended on the leaf reflectance spectrum $[\rho_{\rm L}(\lambda)]$ normalized to the horizontally projected silhouette of leaf area at z $[l_{\rm p}(z)]$ and the average cosine for downwelling irradiance $[\overline{\mu}_{\rm d}(z)]$:

$$\rho_{\rm d}(\lambda, z) = \rho_{\rm L}(\lambda) \cdot \frac{l_{\rm p}(z)}{\overline{\mu}_{\rm d}(z)} \tag{12}$$

The computation of $l_p(z)$ from leaf morphometrics, shoot density, and leaf bending angle is detailed in Zimmerman (2003b, 2006). The amount of light transmitted through

layer (z) was controlled by the exponential loss term $\left[-\left\{a_{\rm L}(\lambda)\cdot t_{\rm L}+a_{\rm epi}(\lambda)\right\}\cdot \frac{l_{\rm p}(z)}{\overline{u}_{\rm d}(z)}-K_{\rm d}(\lambda,z)\cdot \Delta z\right]$ that included both canopy and water column effects. Canopy effects were defined by the leaf- and epiphyte-specific absorption coefficients $[a_L(\lambda)]$ and $a_{epi}(\lambda)$, respectively, the leaf thickness (t_L) , and the horizontally projected leaf area $[l_p(z)]$ at each depth. Absorption by the epiphyte layer can have a strong spectral component, particularly when it is dominated by algae (Drake et al. 2003). However accumulated sediments and detritus tend to flatten the spectrum, especially in turbid estuarine environments. For these simulations, epiphytes were assumed to be neutral density attenuators. Absorption by epiphytes (a_{epi}) was calculated as a function of epiphyte density on the leaf surface (mg cm⁻²) based on the data in fig. 4 of Bulthuis and Woelkerling (1983), but with the regression forced through the origin (0 epiphyte absorption at 0 epiphyte density):

$$a_{\rm epi} = 0.873 \cdot \rm Epi \tag{13}$$

The value of the average cosine $[\overline{\mu}_d(z)]$ was approximated assuming that scattering induced by the canopy was hemispherically isotropic (bi-Lambertian) about the leaf surface (Shultis and Myneni 1988) such that $\overline{\mu}_d(z)$ became increasingly isotropic [i.e., $\overline{\mu}_d(z) \to 0.5$] in proportion to the horizontally projected leaf area in each layer through which the light passed. This caused $K_d(\lambda,z)$ to increase with depth through the submerged plant canopy (Zimmerman 2003b).

On reaching the sea floor, a portion of the light was reflected back in the upward direction. This reflected light was then attenuated by the submerged plant canopy and water column along its path back to the sea surface in a process symmetrical to that for downwelling irradiance:

$$E_{\mathbf{u}}(\lambda, z) = \{ [E_{\mathbf{d}}(\lambda, z) \cdot \rho_{\mathbf{d}}(\lambda, z+1)] + E_{\mathbf{u}}(\lambda, z+1) \} \cdot [1 - \rho_{\mathbf{u}}(\lambda, z)] \cdot \exp \left[- \left\{ a_{\mathbf{L}}(\lambda) \cdot t_{L} + a_{\mathbf{epi}}(\lambda) \right\} \cdot t_{\mathbf{L}} \cdot \frac{l_{\mathbf{p}}(z)}{\overline{\mu}_{\mathbf{u}}} - K_{\mathbf{u}}(\lambda) \cdot \Delta z \right]$$

$$(14)$$

The two-flow approach summarized by Eqs. 11 and 14 provided a mechanistic link between in-canopy light fields and the vertical distribution of the horizontally projected leaf area index, or biomass, of the canopy, which was a function of leaf orientation as well as leaf morphology and shoot density (Zimmerman 2003b).

Photosynthesis of the submerged plant canopy

Calculation of the photosynthetically used radiation [PUR(z)], which was less than the total irradiance attenuated by the canopy that included losses due to reflections from

the leaf surface $(\rho_{\rm d}, \rho_{\rm u})$, epiphyte absorption $(a_{\rm epi})$ and non-specific leaf absorption that did not contribute to photosynthesis, required spectral integration of the total plane irradiance (in quantum units) normalized by the photosynthetic absorptance $[A_{\rm p}(\lambda)]$ of the leaf and the horizontally projected leaf area $[I_{\rm p}(z)]$:

$$PUR(z) = \sum_{\lambda} A_{p}(\lambda) \cdot l_{p}(z) \cdot \left[\frac{E_{d}(\lambda, z-1) \cdot \{1 - \rho_{d}(\lambda)\} \cdot \{1 - A_{epi}(\lambda)\}}{\overline{\mu}_{d}(z-1)} + \frac{E_{u}(\lambda, z+1) \cdot \{1 - \rho_{u}(\lambda)\} \cdot \{1 - A_{epi}(\lambda)\}}{\overline{\mu}_{u}(z+1)} \right]$$

$$(15)$$

PUR(z) was used to drive the instantaneous photosynthetic rate of layer (z) using the cumulative one-hit Poisson function, which provided a quasi-mechanistic relationship between photosynthetic yield and the amount of light absorbed by the leaf (Falkowski and Raven 2007):

$$P(z) = l(z) \cdot P_{E} \cdot \left\{ 1 - \exp\left[-\frac{\phi_{p} \cdot PUR(z)}{P_{E}} \right] \right\}$$
 (16)

In this relation, $P_{\rm E}$ was the irradiance-saturated rate of biomass-specific photosynthesis and $\phi_{\rm p}$ was the quantum yield of photosynthesis (1/8 mol C mol⁻¹ PUR).

Effect of OC on photosynthesis

Light-saturated photosynthesis ($P_{\rm E}$) of eelgrass increases in response to the concentration of DIC in seawater (Zimmerman et al. 1997; Invers et al. 2001; McPherson et al. 2015). In the case of eelgrass, the effect of DIC was quantified using a modified Michaelis–Menten formulation that accounted for the combined effects of [${\rm CO}_{2({\rm aq})}$] and [${\rm HCO}_3^-$] on irradiance-saturated photosynthesis ($P_{\rm E}$) (McPherson et al. 2015):

$$P_{E} = P_{m(HCO_{3}^{-})} \cdot \frac{[HCO_{3}^{-}]}{K_{s(HCO_{3}^{-})} + [HCO_{3}^{-}]} + P_{m(CO_{2(aq)})}$$
$$\cdot \frac{[CO_{2(aq)}]}{K_{s(CO_{2(aq)})} + [CO_{2(aq)}]}$$
(17)

where $P_{\mathrm{m(HCO_3^-)}}$ and $P_{\mathrm{m(CO_{2(aq)})}}$ represented the maximum rate of light- and flow-saturated photosynthesis for the DIC substrates bicarbonate (HCO $_3^-$) and aqueous dissolved carbon dioxide [CO $_{2(aq)}$] respectively; $K_{\mathrm{s(HCO_3^-)}}$ and $K_{\mathrm{s(CO_{2(aq)})}}$ represented the corresponding half-saturation constants. Although [CO $_{2(aq)}$] has a particularly strong effects on eelgrass leaf photosynthesis, it has no measurable effect on

eelgrass respiration over the range of concentrations simulated here (Zimmerman et al. 1997).

Modeling the effect of temperature on photosynthesis, respiration and whole-plant carbon balance

The effect of temperature on leaf photosynthesis is CO_2 dependent such that the Q_{10} for eelgrass P_E is < 2 in the present-day ocean, while the Q_{10} for respiration (R) is about 2.6 (Zimmerman et al. 1989). This causes respiration to rise more rapidly in response to temperature than carbon-limited photosynthesis, potentiating negative daily carbon balances during warm periods. However, OA/OC can reduce the unbalanced effect of temperature on P_E and R because CO_2 stimulation of P_E increases the photosynthetic Q_{10} as an exponential function of $[CO_{2(aq)}]$:

Photosynthetic
$$Q_{10} = 3.62 + 0.796 \cdot \ln \left(\frac{[CO_{2(aq)}]}{9.8 \times 10^9} \right)$$
 (18)

Although salinity and temperature have considerable effects on the air-saturated value of $[CO_{2(aq)}]$, their impacts on Photosynthetic Q_{10} are dampened by the logarithmic relationship with $[CO_{2(aq)}]$ such that Q_{10} can be approximated as a linear function of pH for salinities between 20 and 35 (PSS) and temperatures between 0°C and 30°C:

Photosynthetic
$$Q_{10} = 3.62 - 0.2 \cdot \text{pH}$$
 (19)

Temperatures above 30°C are likely to have acute negative effects on plant metabolism, and are beyond the scope of the present simulation.

Instantaneous whole canopy production [$P_c(t)$] was calculated for each temperature, CO₂, water quality and depth scenario by numerical integration of P(z) over all layers (z):

$$P_{\rm c}(t) = \sum_{z} P(z) \tag{20}$$

Daily production (P_d) of the canopy was calculated by numerical integration of P_c over the photoperiod determined by date and location, using a time step of 10 min assuming the daily variation in $[E_d(\lambda,0^-)]$ was sinusoidal function of photoperiod (cloudless atmosphere):

$$P_{\rm d} = \sum_{t} P_{\rm c}(t) \tag{21}$$

The resulting photosynthesis rates were used to determine whole plant carbon balance by normalizing $P_{\rm d}$ to the daily (24 h) respiratory demand:

Daily
$$P: R = \frac{P_d}{R_d}$$
 (22)

The Daily P:R provides a convenient index of whole plant or canopy production. Survival was possible when Daily $P:R\geq 1$. Conversely long-term survival was impossible when Daily P:R<1. Aerobic respiratory demand of leaves, roots, and rhizomes was scaled to $P_{\rm E}$ at 15°C, $p{\rm CO}_2=400$ $\mu{\rm Atm}$ (Zimmerman et al. 1989):

$$R_{\text{Leaf}} = 0.2P_{\text{E}} \tag{23}$$

$$R_{\text{Root}} = 0.5R_{\text{Leaf}} \tag{24}$$

$$R_{\rm Rhiz} = 0.5 R_{\rm Root} \tag{25}$$

and responded to temperature with a Q_{10} of 2.6 (Zimmerman et al. 1989). For a given temperature regime, nighttime respiration of roots and rhizomes was reduced to 65% of the aerobic (daytime) rate to account for the reverse Pastéur effect observed when these tissues become anoxic (Smith et al. 1988; Smith 1989). Consequently, daily whole plant respiration was calculated as the sum of daily respiratory rates for each of the different tissue components scaled to the shoot: root ratio (σ) , which was set to 3.1 for these simulations:

$$R_{\rm d} = 24 \cdot R_{\rm Leaf} + \left\{ \frac{D \cdot (R_{\rm Root} + R_{\rm Rhiz}) + 0.65 \cdot (24 - D) \cdot (R_{\rm Root} + R_{\rm Rhiz})}{\sigma} \right\}$$
(26)

 $R_{\rm d}$ is relatively insensitive to variations in σ between 1 and 4 because leaves represent the majority of the respiratory load (Zimmerman 2003a).

Analysis of model sensitivity to many of the required parameters can be found in the publications cited above. The analysis presented here will concentrate on the sensitivity of model predictions to the new features created by our integration of water quality and canopy bio-optics with whole plant physiology, in particular the ability of this model to predict (i) $K_{\rm d}(\lambda)$ from Chl a and TSM, and (ii) the interactive effects of temperature, CO₂ and epiphyte load on eelgrass carbon balance and subsequent distribution across the submarine landscape in the context of a changing climate.

Methods and materials

Selection of field sites for validation of model predictions

The ability of the bio-optical model to predict the distribution of eelgrass across the submarine landscape was

evaluated at two locations with contrasting histories of SAV abundance and distribution. The Goodwin Islands, located at the mouth of the York River (37.2167° N 76.4000° W), represented a stressful water quality environment for SAV on the western shore of the Chesapeake Bay. SAV, primarily eelgrass (Zostera marina L.) and widgeon grass (Ruppia maritima L.) cover about 120 ha of nearshore sandy habitat to about 1 m depth. Temporal variation in SAV distribution is high at this site, being affected by low water transparency, epiphyte load, and periodic thermal stress during warm summers (Moore 2004; Moore and Jarvis 2008). The second field site was South Bay (37.2667° N, 75.8167° W), a shallow coastal lagoon in the lee of Wreck Island on the seaward shore of the DelMarVa Peninsula that has experienced a highly successful eelgrass restoration effort now covering > 700 ha (Orth et al. 2006a). South Bay is tidally flushed by relatively clean waters of the mid-Atlantic Ocean that renders it less affected by eutrophication and summer thermal stress than in the Chesapeake Bay.

Bathymetric and optical characterization of the field sites

Acoustic surveys of both sites were conducted between May 2011 and October 2011 using a Humminbird Model 998 multibeam sonar/chartplotter system with integrated GPS receiver mounted to a 5.3 m skiff powered by an outboard engine. All soundings were corrected to MLW using local tide heights measured concurrently with the surveys. Digital elevation models (DEMs), necessary for predictive modeling of eelgrass distribution across the submarine land-scape, were generated by interpolation of the sounding tracks using inverse distance weighting criteria.

Non-water absorption $[a_{\rm t}(\lambda)-a_{\rm w}(\lambda)]$ and scattering coefficients $[b(\lambda)]$ used to parameterize the model were measured at various stages of the tide and times of day at both sites between May 2011 and October 2011 using an ac-9 submersible spectrophotometer (WetLabs). Instrument values were corrected for ambient temperature, salinity, and total scattering (Pegau et al. 2003). The backscatter coefficient $[b_{\rm b}(555)]$ was measured using a HydroScat-6 (HOBI Labs) and corrected for total scattering and absorption (Maffione and Dana 1997). Diffuse spectral attenuation coefficients $[K_{\rm d}(\lambda)]$ were determined according to the Lambert–Beer Law from simultaneous measures of downwelling spectral irradiance $[E_{\rm d}(\lambda,z)]$ offset by a vertical distance of 0.5 m using a 4-channel HydroRAD spectroradiometer system (HOBI Labs).

Absorption coefficients for phytoplankton (a_ϕ) and nonalgal particles $(a_{\rm p-\phi})$ were measured spectrophotometrically from bulk water samples captured onto GF/F filters under gentle vacuum. The filtrate was collected directly into acid washed borosilicate glass vials and subsequently passed through acid-washed, 0.2 μ m polycarbonate filters. CDOM absorbance of the second filtrate was measured against Nanopure water using a Shimadzu UV2401 scanning spectrophotometer (10 cm path). CDOM absorbances were corrected for

scattering and converted to absorption coefficients [$a_g(\lambda)$, uni $ts = m^{-1}$] (Mitchell et al. 2002). Spectral absorption coefficients of particles collected on the GF/F filters were measured against a clean filter moistened with Nanopure water using an integrating sphere attached to the spectrophotometer and corrected for multiple scattering (Cleveland and Weidemann 1993). Non-algal particulate absorption was measured spectrophotometrically on the same filters after extracting the pigments in 90% methanol for 12 h. Chlorophyll a (Chl a) was extracted from companion filters using sonication in ice-cold 90% acetone and quantified spectrophotometrically (Jeffrey and Humphrey 1975). TSM concentrations were determined by filtering measured volumes of the same bulk water samples onto preweighed Nucleopore filters (0.2 μ m pore size). The filters were rinsed with deionized water to remove salts, dried at 60°C for 5 d and reweighed. The concentration of suspended mass in the water was calculated by normalizing the mass captured to the volume filtered.

Projecting eelgrass distributions for different climate scenarios

The governing equations described above were translated into Fortran as a set of coupled subroutines with userinterface that we refer to as GrassLight Ver. 2.11. A 64-bit executable version of the model was generated for these calculations using the Intel Visual Fortran Compiler (Ver. 12.1.0.2). The original source code, compiled executable versions for 32-bit and 64-bit Windows operating systems, and a user guide are freely available from the authors on request. The GrassLight model was run iteratively to determine the maximum shoot density where Daily P: R = 1 for a range of depths between 0 m and 2 m (MLW) on the summer solstice for both sites. Temperatures were selected to simulate a cool summer (25°C) below the threshold for thermal stress and a warm summer (30°C) known to cause thermal stress in eelgrass. CO₂ concentrations were simulated for the present day (roughly 2011), mid-century (roughly 2050), and end-of-century (roughly 2100), based on IPCC (2013) projections. For all runs, the specified [CO_{2(aq)}] and pH were determined by CO2SYS (Lewis and Wallace 1998) using measured values of salinity and alkalinity for both sites, and average pCO_2 concentrations for the present day, mid-century and end-of century [Table 2; IPCC (2013)]. Optical properties of eelgrass leaves were averaged from > 500 spectral measurements (Cummings and Zimmerman 2003; Zimmerman 2003b). The resulting relationship between depth and eelgrass density produced a unique "sparse model" for each simulated environment consisting of a quadratic function that quantified eelgrass density as a function of water depth. Eelgrass densities predicted from the sparse model relationships were then mapped across DEMs of the submarine landscape generated for Goodwin Islands and South Bay.

Table 2. Parameter values assigned to each *GrassLight* simulation. All runs were conducted for the summer solstice (14.5 h photoperiod) using mean concentrations of Chl a, TSM, and CDOM absorption [$a_g(440)$] measured at both sites. Temperatures were selected to simulate a cool summer (25°C) below the threshold for thermal stress and a warm summer (30°C) known to cause thermal stress in eelgrass. CO₂ concentrations were simulated for the present day (roughly 2011), mid-century (roughly 2050), and end-of-century (roughly 2100), based on IPCC (2013) projections. Concentrations of dissolved aqueous CO₂ and seawater pH were determined from CO2SYS (Lewis and Wallace 1998) using values of temperature, salinity, alkalinity, and pCO₂ indicated below. When not listed, parameter values for warm simulations were the same as listed for Cool 2011 simulations.

Climate	Cool 2011	Warm 2011	Warm 2050	Warm 2100
	C001 2011	2011	2030	2100
All simulations	145			
Day Length (h)	14.5	20	20	20
Temperature (°C)	25	30	30	30
pCO_2 (μ Atm)	400	400	600	870
$P_{m(HCO_3^-)}$ (relative units)	1			
$P_{m(CO_2)}$ (relative units)	6.3			
$K_{s(HCO_3^-)}(\mu mol L^{-1})$	1400			
$K_{s(CO_{2(aq)})}(\mu mol L^{-1})$	800			
Leaf Epiphyte Load	0 and 1.24 f	rom Moor	e (2004)	
(mg cm ⁻²)				
Shoot:Root Ratio	3.1			
Canopy Orientation	10° from	vertical		
Goodwin islands				
Salinity (PSS)	20			
Alkalinity (μEquiv kg ⁻¹ S	W) 1500			
рН	8.10	8.11	7.95	7.80
$[CO_{2(aq)}]$ (μ mol L ⁻¹)	12.2	10.8	16.2	23.5
$[HCO_3^-]$ (μ mol L ⁻¹)	1294	1260	1324	1370
Chl a (mg m ^{-3})	9.0 ± 1.6			
TSM (mg L^{-1})	8.4 ± 2.7			
$a_{\rm g}(440)~({\rm m}^{-1})$	$\boldsymbol{0.372 \pm 0.07}$			
Canopy Height (m)	0.1			
Shoot Leaf Area	0.001			
$(m^2 shoot^{-1})$				
South Bay				
Salinity (PSS)	30			
Alkalinity (μ Equiv kg ⁻¹ S	W) 2200			
рН	8.19	8.20	8.00	7.91
$[CO_{2(aq)}]$ (μ mol L ⁻¹)	11.6	10.3	15.4	22.4
[HCO $_3$] (μ mol L $^{-1}$)	1748	1685	1806	1900
Chl a (mg m ⁻³)	3.7 ± 1.0			
TSM (mg L^{-1})	6.5 ± 3.5			
$a_{\rm q}(440)~({\rm m}^{-1})$	0.212 ± 0.04			
Canopy Height (m)	0.25			
Shoot Leaf Area	0.0047			
$(m^2 shoot^{-1})$				

Statistical analyses and field validation of model predictions

Quantitative relationships among measured variables were determined using least squares regression routines implemented in Microsoft Excel (Ver. 14.0.7140.500) and Analysis of Covariance (ANCOVA) routines implemented in MathWorks Matlab R2012b (8.0.0.783). Accuracy of $K_{\rm d}(\lambda)$ values predicted from measured values of [Chl a], [TSM] and $a_{\rm g}(\lambda)$ were compared against radiometrically determined observations of $K_{\rm d}(\lambda)$ measured by the Hydro-RAD simultaneously with the collection of water samples used to measure the water quality parameters. The wavelength-specific root mean square deviation [RMSD(λ), units = m⁻¹] between measured and modeled $K_{\rm d}(\lambda)$ was calculated as:

$$RMSD(\lambda) = \sqrt{\frac{\sum_{n} \left[K_{d}(\lambda)_{\text{measured}} - K_{d}(\lambda)_{\text{modeled}} \right]^{2}}{n-1}}$$
 (27)

where n represented the number of spectral observations. Normalized RMS deviations (NRMSD, dimensionless) were obtained by dividing RMSD(λ) by the range of measured values at each wavelength:

$$NRMSD(\lambda) = \frac{RMSD(\lambda)}{K_d(\lambda)_{max} - K_d(\lambda)_{min}}$$
(28)

Maps of eelgrass distribution produced from a combination of aerial imagery and ground-based field observations by the SAV Program, Virginia Institute of Marine Science (Orth et al. 2012, http://www.vims.edu/bio/sav) were used to validate GrassLight predictions of eelgrass density and distribution at both sites for the relatively cool 2011 growing season. Epiphytes represent a particularly important structuring element of the eelgrass meadow at Goodwin Islands and the York River estuary (Neckles et al. 1993; Neckles et al. 1994; Moore 2004), and we compared the VIMS map against our model simulation of eelgrass distribution and density that incorporated the effect of a mean epiphyte load reported by Moore (2004) for the Goodwin Islands. Epiphytes are less abundant at South Bay (R. J. Orth pers. comm. and our personal observations); consequently we compared the VIMS map to our cool climate 2011 scenario for that site without epiphytes. ArcGIS shapefiles containing polygons of SAV bed density (VIMS % cover classes) for 2011 were downloaded from the VIMS website and converted to a raster matrix of grid points spaced at 10 m intervals. Leaf area indices (L_{pred}) predicted by Grass-Light at the same grid points were converted to horizontally projected estimates of %Cover based on the same geometric reasoning used to calculate the horizontally projected leaf area (l_p) in each layer of the canopy (Zimmerman 2003b, 2006), in which the bending angle (β) of the canopy

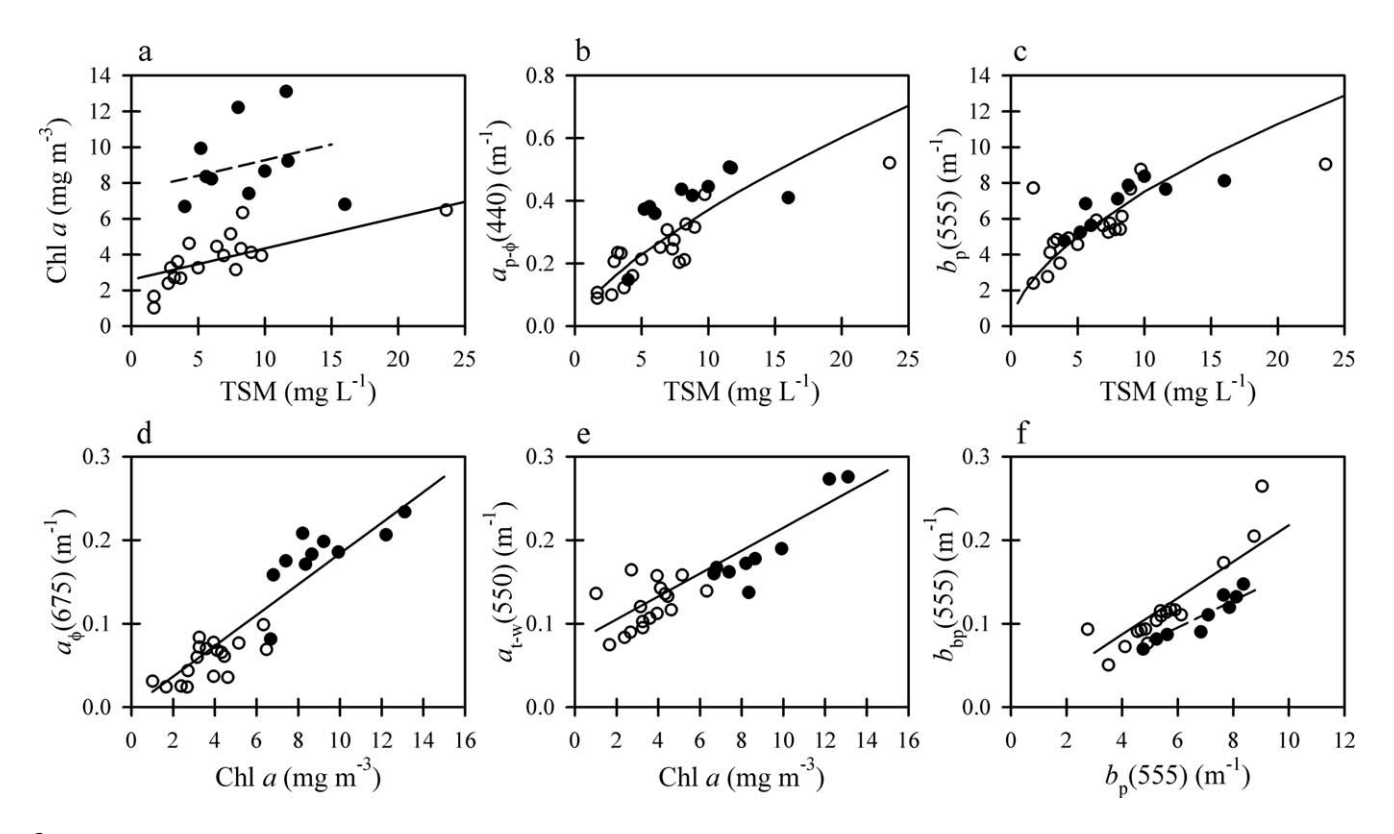


Fig. 1. Relationships between IOPs, concentrations of TSM and Chl *a* at the Goodwin Islands (closed circles, all plots) and South Bay (open circles, all plots). Lines indicate the relationships between plotted variables, as determined by ANCOVA and regression analyses (Table 3). Dashed lines in Fig. 1a,f indicate the relationships among variables for Goodwin Islands. Solid lines in Fig 1a,f indicate significantly different relationships among the same variables for South Bay. Solid lines in Fig 1b,c,d,e indicate overall relationships between variables when no differences between Goodwin Islands and South Bay were detected by ANCOVA.

determines the percent of surface area occupied by eelgrass when viewed from above:

$$\% \operatorname{Cover} = 100 \cdot L_{\operatorname{pred}} \cdot \sin(\beta) \tag{29}$$

The bending angle of the vertically distributed plant canopy was set to 10° from vertical for all simulations, which represents the optimum orientation to maximize whole canopy photosynthesis and minimize self-shading (Zimmerman 2003b). The resulting estimates of %Cover were then binned to the 4 density classes defined by the VIMS SAV Program. Error matrices were computed to compare the spatial distribution of observed density against the distributions generated from quadratic sparse models mapped across the DEMs.

Results

Predicting the distribution of downwelling irradiance from water quality measures

The relationships between IOPs and the standard water quality monitoring parameters (TSM, Chl a) showed a wide range of similarities, and a few important differences

between Goodwin Islands and South Bay. Concentrations of TSM ranged from < 5 mg L^{-1} to > 15 mg L^{-1} at both sites, and mean concentrations were not significantly different between sites. However, the average Chl a concentration was 2.4-fold higher at Goodwin Islands $(9.0 \pm 1.64 \text{ mg m}^{-3})$ than South Bay $(3.7 \pm 0.45 \text{ mg m}^{-3})$, even though the slope of the Chl a vs. TSM relationship was statistically indistinguishable between the sites (Fig. 1a; Table 3). Although the regressions did not have a lot of predictive power ($r^2 = 0.24$ for Goodwin Islands and 0.56 for South Bay), they point to a significant difference in the composition of suspended particles between the two sites that may affect the IOP-based parameterizations required for the bio-optical model. Despite this difference in Chl a vs. TSM, relations between all optical properties required to parameterize the optical model were statistically indistinguishable between sites with the exception of $b_{\rm bp}(555)/b_{\rm p}(555)$. The relationship between absorption by non-algal particles $[a_{p-\phi}(440)]$ and TSM followed a single power function defined by Eq. 6 (Fig 1b; Table 4; a*_p-\(\phi \) (440) = 0.074, $v_{sa} = 0.70$, $r^2 = 0.69$), even though the mean value of $a_{p-\phi}(440)$ was significantly higher at Goodwin Islands (0.39 ± 0.03) than South Bay (0.24 ± 0.03) (Table 4). The relationship between total particulate scattering

Table 3. Analysis of Covariance (ANCOVA) summary tables comparing relationships among biogeochemical and optical properties at Goodwin Islands and South Bay illustrated in Fig. 1, **Chl a vs. TSM ANCOVA**

Source	df	Sum Sq.	Mean Sq.	F	Prob > <i>F</i>
Location	1	148.39	148.39	62.13	< 0.001
TSM	1	16.69	16.69	6.99	0.014
$Location \times TSM$	1	2.71	2.71	1.13	0.297
Error	24	57.32	2.39		

No significant difference in slopes between Goodwin Islands and South Bay.

Term	Estimate	Std. Err.	t	Prob> t
Intercept	5.071	0.586	8.650	< 0.001
South Bay	2.599	0.314	-7.861	< 0.001
Goodwin Isl.	7.543	0.314	7.861	< 0.001
Slope	0.174	0.066	2.637	0.014

Assuming parallel slopes, intercept for Goodwin Islands was significantly higher.

Source	df	Sum Sq.	Mean Sq.	F	Prob>F
Location	1	148.39	148.39	61.80	< 0.001
TSM	1	16.69	16.69	6.95	0.014
Error	25	60.03	2.40		

Conclusion: mean Chl a concentration was higher at Goodwin Islands, and constituted a larger fraction of TSM than at South Bay.

Table 4. Analysis of Covariance (ANCOVA) summary tables comparing relationships among biogeochemical and optical properties at Goodwin Islands and South Bay illustrated in Fig. 1, Non-algal particulate absorption [$a_{p-\phi}$ (440)] vs. TSM ANCOVA:

Source	df	Sum Sq.	Mean Sq.	F	Prob>F
Location	1	0.09	0.09	19.80	< 0.001
TSM	1	0.20	0.20	46.35	< 0.001
$Location \times TSM$	1	0.00	0.00	0.08	0.783
Error	25	0.11	0.00		

No significant difference in slopes between Goodwin Islands and South Bay.

Term	Estimate	Std. Err.	t	Prob> t
Intercept	0.174	0.024	7.143	< 0.001
South Bay	0.115	0.013	-4.531	< 0.001
Goodwin Isl.	0.233	0.013	4.531	< 0.001
Slope	0.019	0.003	6.932	< 0.001

Assuming parallel slopes, intercept for Goodwin Islands was significantly higher.

Source	df	Sum Sq.	Mean Sq.	F	Prob>F
Location	1	0.09	0.09	20.53	< 0.001
TSM	1	0.20	0.20	48.05	< 0.001
Error	26	0.11	0.00		

Conclusion: The relationship between $a_{p-\phi}$ (440) and TSM was constant across both sites, but mean $a_{p-\phi}$ (440) was higher at Goodwin Islands.

Table 5. Analysis of Covariance (ANCOVA) summary tables comparing relationships among biogeochemical and optical properties at Goodwin Islands and South Bay illustrated in Fig. 1, **TSM vs.** b_n (555) **ANCOVA**

Source	df	Sum Sq.	Mean Sq.	F	Prob>F
Location	1	4.356	4.356	2.943	0.099
TSM	1	37.244	37.244	25.163	< 0.001
$Location \times TSM$	1	0.058	0.058	0.039	0.844
Error	24	35.523	1.480		

No significant difference in slopes between Goodwin Islands and South Bay.

Term	Estimate	Std. Err.	t	Prob> t
Intercept	4.217	0.451	9.350	< 0.001
Goodwin Isl.	3.787	0.246	-1.750	0.092
South Bay	4.647	0.246	1.750	0.092
Slope	0.262	0.051	5.116	< 0.001

Assuming parallel slopes, no significant difference in intercepts.

Source	df	Sum Sq.	Mean Sq.	F	Prob>F
Location	1	11.105	11.105	3.965	0.057
Error	26	72.825	2.801		
Assuming the a singl	e relationship, no signif	icant difference in mean valu	es of bp(555).		

Conclusion: The relationship between TSM and b_p (440) was constant across both sites.

Table 6. Analysis of Covariance (ANCOVA) summary tables comparing relationships among biogeochemical and optical properties at Goodwin Islands and South Bay illustrated in Fig. 1, **Chl a concentration vs. Total absorption** $[a_{gp}(555)]$ **ANCOVA:**

Source	df	Sum Sq.	Mean Sq.	F	Prob>F
Location	1	0.005	0.005	3.71	< 0.001
Chl	1	0.033	0.033	25.31	< 0.001
$Group{ imes}Chl$	1	0.000	0.000	0.03	0.8619
Error	23	0.030	0.001		

Assuming intercepts = 0, slopes are not significantly different.

Term	Estimate	Std. Err.	t	Prob> t	
Intercept	0.161	0.010	15.825	< 0.001	
South Bay	0.132	0.010	-2.896	0.008	
Goodwin Isl.	0.190	0.010	2.896	0.008	
But mean [Chl a] is significantly higher at Goodwin Island.					

Conclusion: Overall trend is best explained by a single regression line.

 $[b_{
m p}(555)]$ and TSM also followed a single power function described by Eq. 9 for both sites combined (Fig. 1c; Table 5; $b_{
m p}^{\star}(555)=1.94,\ v_{
m sb}=0.59,\ r^2=0.81).$ Further, the mean value of particulate scattering $[b_{
m p}(555)]$ for Goodwin Islands was not significantly different from the value at South Bay (Table 5). The relationship between phytoplankton absorption $[a_{\phi}(675)]$

Table 7. Analysis of Covariance (ANCOVA) summary tables comparing relationships among biogeochemical and optical properties at Goodwin Islands and South Bay illustrated in Fig. 1, Particulate Backscatter Coefficient $[b_{bp}(555)]$ vs. Particulate Scattering Coefficient $[b_{p}(555)]$ t-test:

Location	Slope	Std. Err	df	Т	Prob>t
South Bay	0.022	0.001	15	5.85	< 0.001
Goodwin Isl.	0.016	0.0005	9		

Assuming intercept = 0, slopes are significantly different. Conclusion: Particulate backscattering [b_{bp} (555)] represents a signifi-

Conclusion: Particulate backscattering [$b_{pp}(555)$] represents a significantly higher fraction of total scattering [$b_{p}(555)$] at South Bay, suggesting a higher mineral content for TSM.

and Chl a produced a single, statistically significant linear relationship ($a_{\phi}^{\star}=0.018\pm0.001$, $F_{\rm reg}=546$, df = 1, 27, p<0.001, $r^2=0.85$) common to both sites assuming a 0 intercept (Fig. 1d). As a result, $v_{\phi}=1$ for all simulations. The relationship between the non-water absorption coefficient [$a_{\rm t-w}(555)$] and Chl a produced a single, statistically significant slope common to both sites, even though Chl a concentrations were significantly higher at Goodwin Islands than South Bay (Fig. 1e; Table 6; $r^2=0.75$). The nonzero intercept of this relationship provided an estimate of the residual absorption due to CDOM and non-algal particles. The slope of the relationship between particulate backscattering and total particulate scattering [$b_{\rm bp}(555)/b_{\rm p}(555)$], however, was significantly higher

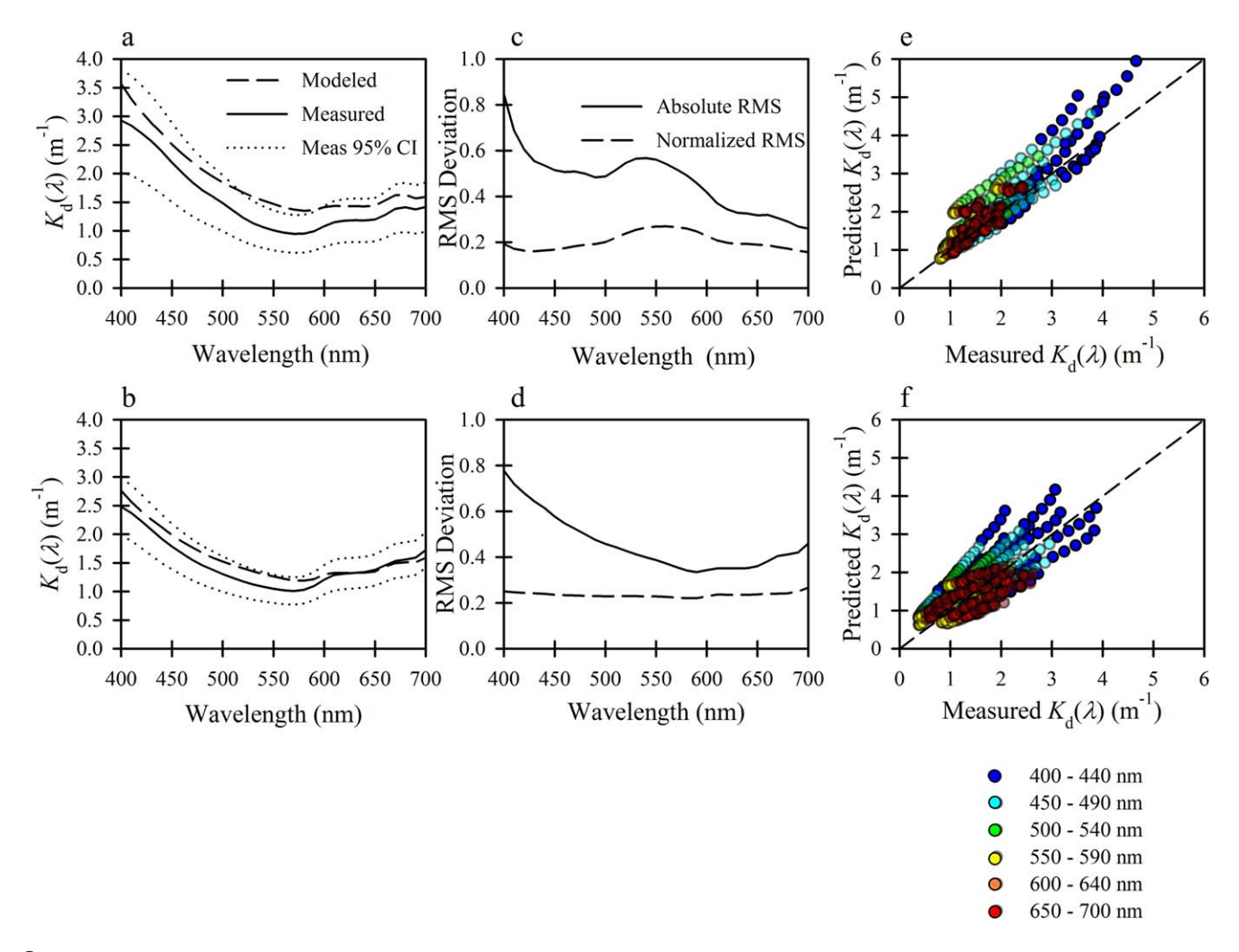


Fig. 2. Measured (solid line) and modeled (dashed line) $K_d(\lambda)$ spectra for (a) Goodwin Islands and (b) South Bay, respectively. Dotted lines indicate 95% confidence intervals around the measured values. RMS deviations for measured vs. modeled spectra for (c) Goodwin Islands and (d) South Bay, respectively. Absolute deviations from measured values (m⁻¹) are indicated by the solid lines. Normalized deviations from measured values (dimensionless) are indicated by the dashed lines. Predicted $K_d(\lambda)$ spectra plotted against measured values for (e) Goodwin Islands and (f) South Bay, respectively. Diagonals (dashed lines) represent lines of perfect agreement (slope = 1, intercept = 0). Colors indicate wavelength range of the individual data points. [Color figure can be viewed in the online issue, which is available at wileyonlinelibrary.com.]

for South Bay than for Goodwin Islands assuming a 0 intercept for both data sets (Fig 1f; Table 7; $r^2 = 0.71$ and 0.81 for Goodwin Islands and South Bay, respectively).

Similarities in relationships among Chl a, TSM and the optical properties described above allowed us to use a common set of parameterizations for the water column equations (Eqs. 1 through 10) required to predict $K_{\rm d}(\lambda)$ at both sites, with the exception of $b_{\rm bp}(555)/b_{\rm p}(555)$, which was set to 0.016 and 0.020 for Goodwin Islands and South Bay simulations, respectively. Resulting spectra of $K_{\rm d}(\lambda)$ predicted from the model using specific values of Chl a and TSM from water samples fell within the 95% confidence limits for simultaneously measured values of $K_{\rm d}(\lambda)$ at both sites (Fig. 2a,b, n=10 and 14 for Goodwin Islands and South Bay, respectively). Mean $K_{\rm d}(\lambda)$ values predicted by the model for

Goodwin Islands were slightly higher than the mean of the measured values, but the RMS deviation between predicted and measured values were within 20% across the spectrum (Fig. 2c). Mean model predictions of $K_{\rm d}(\lambda)$ for South Bay showed less bias in the green portion of the spectrum, and the resulting RMS deviations were also within 20% (Fig. 2b,d). Many of the individually modeled $K_{\rm d}(\lambda)$ spectra showed even better agreement with measured values at both sites, particularly between 450 nm and 650 nm that constitutes most of the light available for photosynthesis in these systems (Fig. 2e,f).

Using mean concentrations of TSM and Chl a, and mean values for CDOM absorption [$a_g(440)$] measured in 2011(Table 2), the depth distributions of spectral quantum irradiance at Goodwin Islands and South Bay were calculated

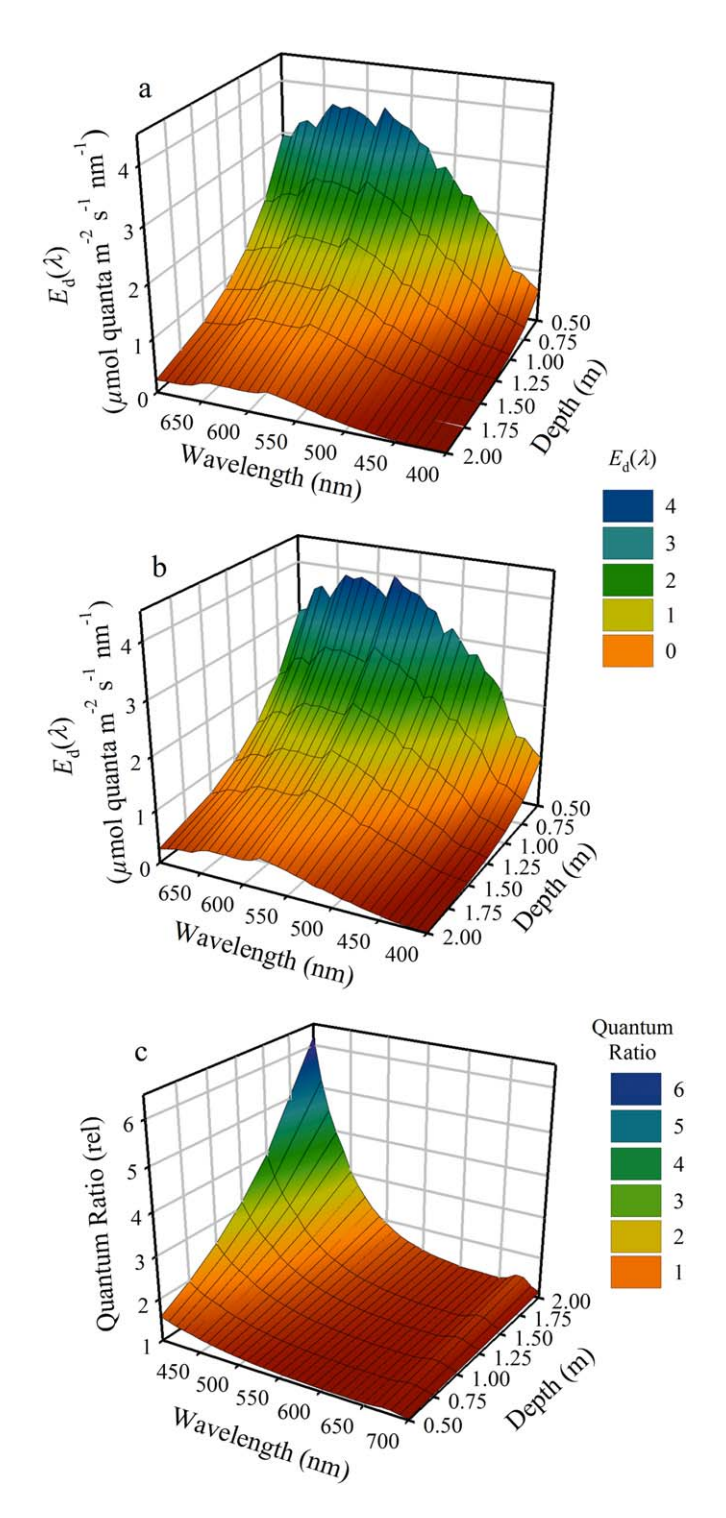


Fig. 3. Depth profiles of spectral irradiance at noon on the summer solstice for (a) Goodwin Islands and (b) South Bay, respectively, derived from mean water column $K_d(\lambda)$ (Fig. 2a,b). (c) Quantum ratio of irradiance spectra (South Bay/Goodwin Islands) plotted as functions of wavelength and depth. Orientations of the wavelength and depth axes were reversed relative to Fig. 3a,b to enhance visual clarity. [Color figure can be viewed in the online issue, which is available at wileyonlinelibrary.com.]

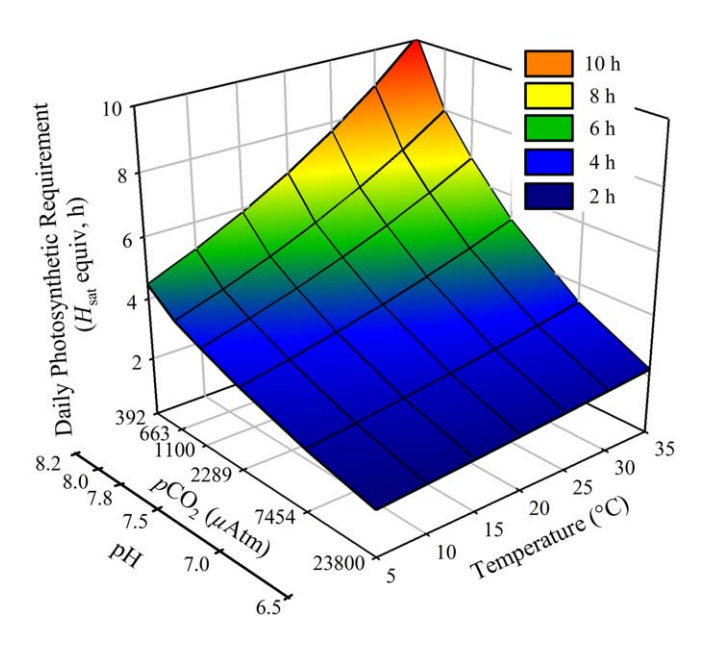


Fig. 4. Combined effects of ambient temperature and CO₂ concentration on the daily photosynthetic requirement to maintain positive whole-plant carbon balance, determined from Eqs. 16–21. [Color figure can be viewed in the online issue, which is available at wileyonlinelibrary.com.]

for local solar noon on the summer solstice (Fig. 3). Although the irradiance spectra were dominated by green wavelengths (500–600 nm) at both sites, higher absorption by Chl a and CDOM at the Goodwin Islands resulted in a higher mean $K_{\rm d}(\lambda)$, and consequently lower spectral irradiances at all depths, relative to South Bay (Fig. 3a vs. 3b). Differences were most pronounced in the blue (400–500 nm) and red (650–700 nm) regions of the spectrum, and the differences increased with depth such that the blue region of the spectrum that is most efficient in driving photosynthesis was nearly two-fold higher at South Bay than at Goodwin Islands at a depth of 0.5 m and more than sixfold higher at 2 m (Fig. 3c).

Sensitivity of eelgrass carbon balance to climate warming and OA/OC

Equations 16 through 26 determined the combined effects of temperature and pCO₂ on the daily integrated photosynthesis required to satisfy the minimum respiratory demand of whole plants (Fig. 4). Requirements were scaled in terms of H_{sat} equivalents, which represented the duration (in hours) of irradiance-saturated photosynthesis $(P_{\rm E})$ required to meet the daily respiratory demand. At a temperature of 10°C, and 2011 pCO2 levels, the respiratory load required the photosynthetic equivalent of 5 h of H_{sat} . A temperature of 30°C, which may be experienced during warm summers, increased the H_{sat} requirement to about 9 h. However, a pCO₂ concentration of 870 μ Atm, which approximates the median IPCC (2013) projection for the end of the 21st Century, raised $P_{\rm E}$ sufficiently to reduce the daily H_{sat} requirement at 30°C to about 4.8 h, thereby lowering the effect of temperature on whole-

Table 8. Quadratic regression coefficients [Maximum Leaf Area Index (L) vs. Depth (z)] and colonization depth limits for each simulation used to create the eelgrass distribution maps (Figs. 6, 7). The resulting vertical distribution of L(z) for each simulation is plotted in Fig. 5.

GrassLight Input Parameters			Sparse Model Polynomial Regression Coefficients, Depth Limits, Areal Coverage, and Median Density					mits, Areal
pCO ₂ (μAtm)	Temperature (°C)	Epiphytes (mg cm ⁻²)	x ² slope	<i>x</i> slope	Biomass Intercept [L(0)]	Depth Limit (m MLW)	Total Area (ha)	Median L (m² m ⁻²)
Goodwin Isl	lands							
400	25	0	1.06	-8.95	10.4	1.4	188	6.2
400	30	0	0.76	-7.80	8.7	1.2	183	5.0
600	30	0	1.05	-8.79	9.9	1.3	186	5.8
870	30	0	1.49	-9.93	11.0	1.4	188	5.7
400	25	1.24	1.66	-8.15	5.9	0.9	154	2.6
400	30	1.24	1.16	-7.19	4.8	0.8	140	2.0
600	30	1.24	1.69	-7.99	5.5	0.9	149	2.4
870	30	1.24	2.06	-8.74	6.2	0.9	156	2.7
South Bay								
400	25	0	0.60	-6.76	9.6	1.7	968	6.1
400	30	0	0.39	-5.90	8.0	1.5	948	5.1
600	30	0	0.50	-6.64	9.4	1.6	960	6.0
870	30	0	0.78	-7.35	10.0	1.7	971	6.3
400	25	1.24	0.81	-6.24	5.8	1.1	775	3.6
400	30	1.24	0.56	-5.53	4.7	0.9	695	3.5
600	30	1.24	0.81	-6.24	5.5	1.0	740	3.0
870	30	1.24	1.01	-6.64	5.9	1.1	766	3.6

plant carbon balance. These relationships provided the metabolic basis for simulating the integrated bio-optical impact on eelgrass carbon balance to different climate scenarios.

Projecting the effects of climate warming and OA/OC onto future eelgrass distributions

Maximum sustainable shoot densities (L_{pred} where Daily P: R=1) predicted for the summer solstice decreased with depth in a slightly nonlinear fashion that was well described by a quadratic function for each simulated environment (Table 8; Fig. 5). In the absence of leaf epiphytes or OA/OC, and with a cool water column (25°C), GrassLight predicted the submarine light environment of Goodwin Islands to support an eelgrass LAI of 10.4 at 0 m depth (intercept, Table 8), with a depth limit for survival of 1.4 m (MLW) (Fig. 5a). Mapping this relationship across the submarine landscape provided by the DEM produced a broad swath of moderately dense eelgrass meadow along the north and eastern shores of the Goodwin Islands, and a rather sharp demarcation where depths exceeded sustainable limits (Fig. 6a). Unvegetated (light blue) areas in close proximity to the shoreline were shallower than 0 m MLW and considered unfavorable for eelgrass colonization. The model predicted a very narrow

band of vegetation along the western shore of Goodwin Islands where the water deepens rapidly into a navigation channel separating the study site from the mainland. An epiphyte density of 1.24 mg cm⁻² leaf, based on average values for the Goodwin Islands eelgrass (Moore 2004), reduced the maximum sustainable LAI by 48% to 5.9 and shoaled the depth limit for eelgrass survival by 40% to 0.9 m (MLW) (Table 8; Fig 5b). This decreased the overall eelgrass density around the island and shoaled the deep edge of the meadow relative to the model scenario without epiphytes (Fig. 6a vs. 6b). In the absence of epiphytes, increasing the temperature to 30°C reduced the supportable eelgrass density by 30% and reduced the depth limit for survival by 20% relative to the cool water simulations (Fig. 6a vs.6c). Elevated temperature reduced eelgrass distribution in the presence of epiphytes by about 20% and the depth limit by 10% relative to the cool water simulation with epiphytes (Figs. 5a vs. 5b, 6b vs. 6d). Raising the pCO₂ to a mid-century level of 600 µAtm (seawater pH 7.95) nearly compensated for the negative effects of thermal stress, increasing the supportable shoot density and depth distribution to within 5% of the present-day cool environment with and without epiphytes (Figs. 5a vs.5b, 6a vs. 6e, 6b vs. 6f). Simulating an end-of-century pCO2 level (870 μ Atm, seawater pH 7.8) under warm summer conditions

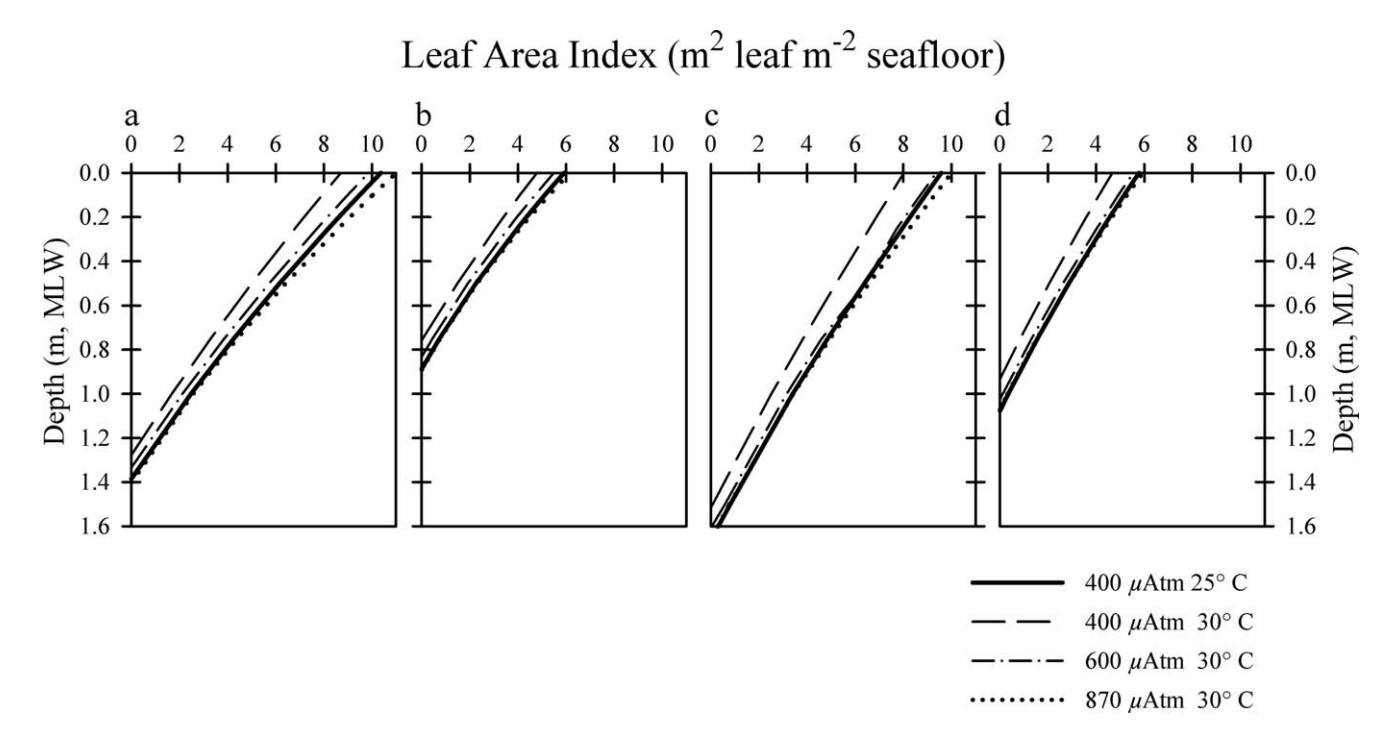


Fig. 5. Maximum sustainable shoot density (defined as Daily P: R = 1) plotted as a function of depth for average water quality conditions and different climate (temperature and pCO_2) scenarios indicated by the legend. (a) Goodwin Islands with no epiphytes. (b) Goodwin Islands with epiphytes. (c) South Bay with no epiphytes. (d) South Bay with epiphytes.

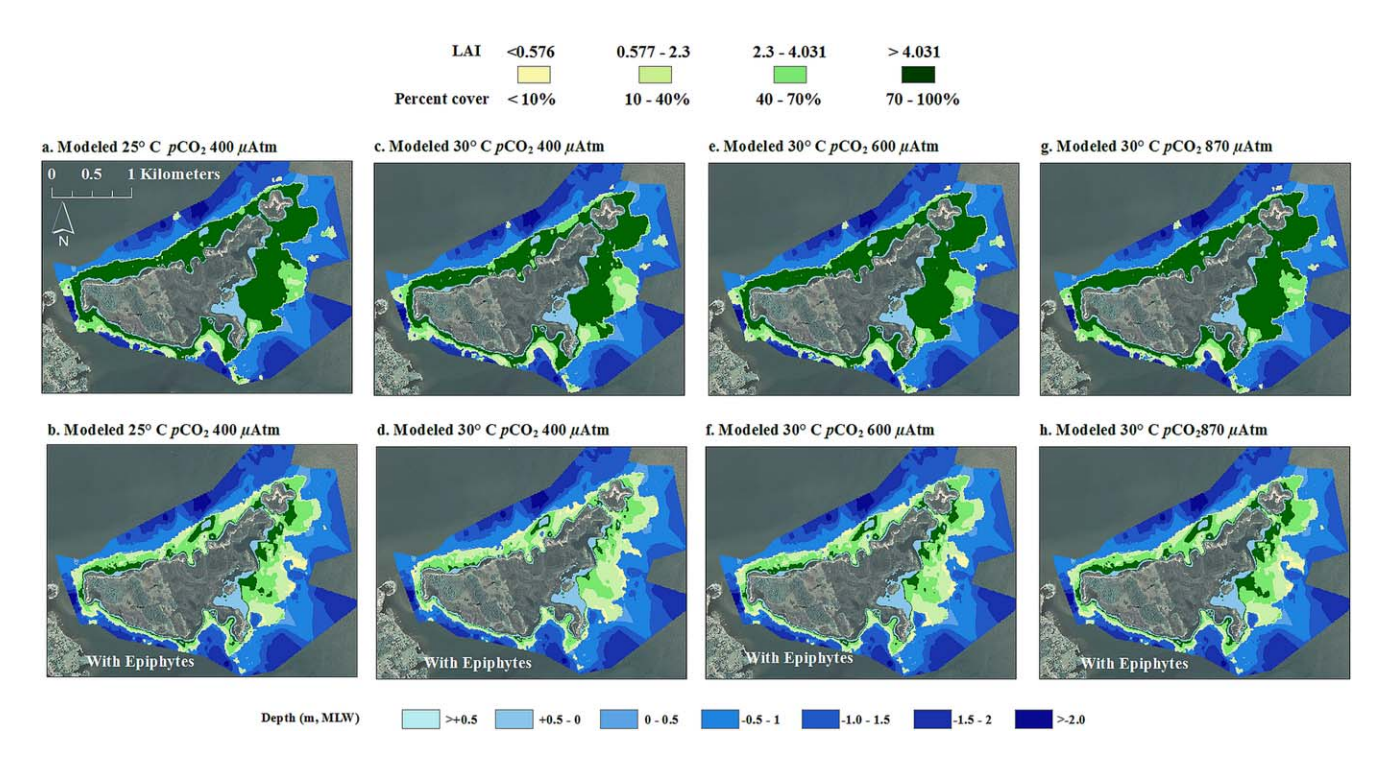


Fig. 6. Combined effects of ambient temperature and pCO_2 on the distribution and density of eelgrass (tan to green colors) across the submarine landscape overlaid on the DEM (blue colors) at Goodwin Islands. Conditions for each simulation are indicated on the plots. Unvegetated light blue areas close to shore represent intertidal regions shallower than 0 MLW, which we considered too shallow for successful eelgrass colonization. Density classes were selected to match the classes defined by the Virginia Institute of Marine Science SAV Program (http://web.vims.edu/bio/sav/). [Color figure can be viewed in the online issue, which is available at wileyonlinelibrary.com.]

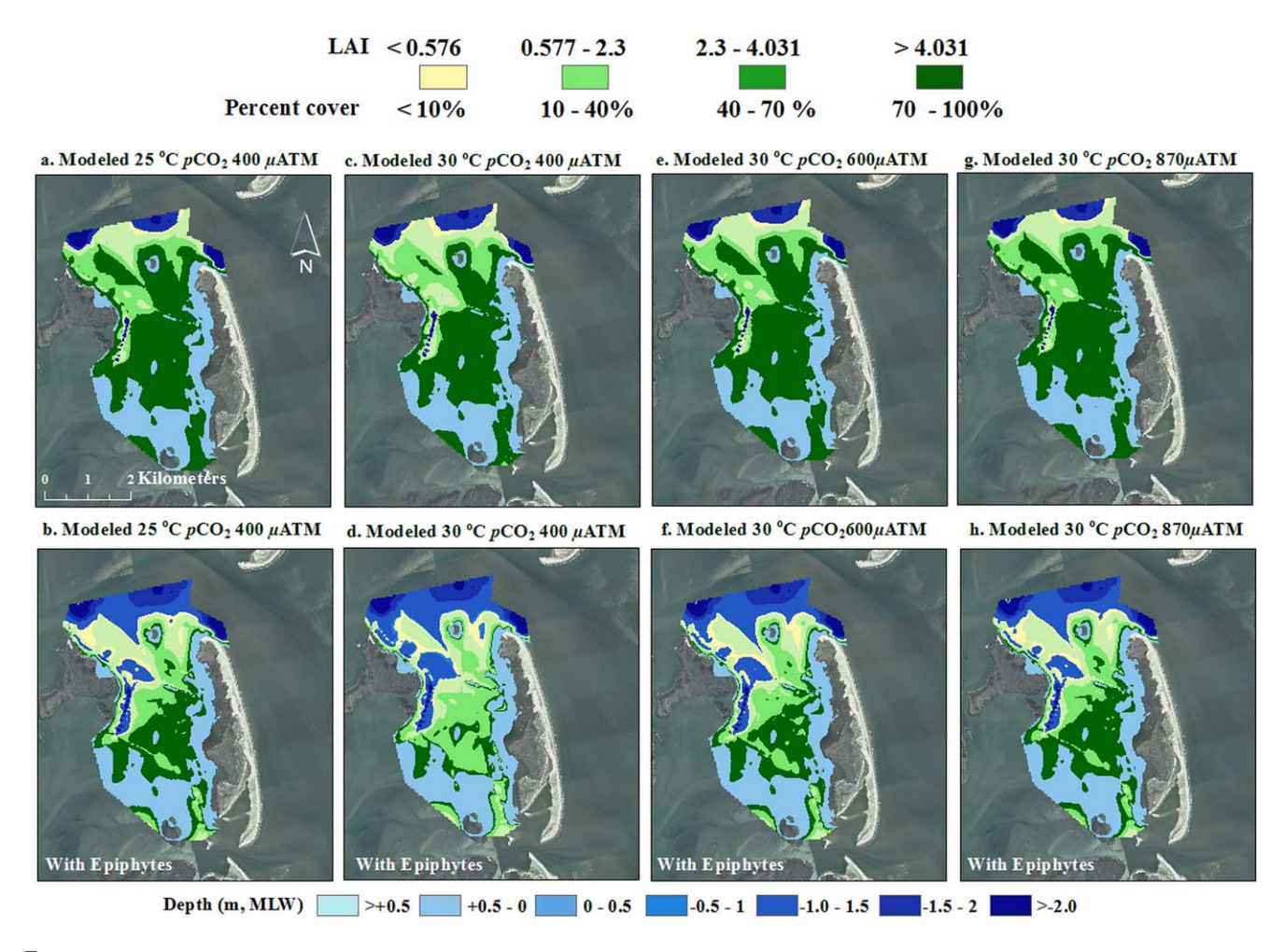


Fig. 7. Combined effects of ambient temperature and pCO_2 on the distribution and density of eelgrass (tan to green colors) across the submarine landscape overlaid on the DEM (blue colors) at South Bay. Conditions for each simulation are indicated on the plots. Unvegetated light blue areas close to shore represent intertidal regions shallower than 0 MLW, which we considered too shallow for successful eelgrass colonization. Density classes were selected to match the classes defined by the Virginia Institute of Marine Science SAV Program (http://web.vims.edu/bio/sav/). [Color figure can be viewed in the online issue, which is available at wileyonlinelibrary.com.]

extended the sustainable density and depth distribution just beyond the present day cool water simulations with and without epiphytes (Figs. 5a,b, 6g,h).

In the absence of any climate impacts on temperature and CO₂ availability, the lower diffuse attenuation coefficients of South Bay produced a range of eelgrass densities similar to those predicted for Goodwin Islands but the depth limit (1.7 m) was 21% deeper (Table 8; Fig. 5a vs. 5c). Mapping this distribution across the submarine landscape of South Bay revealed a broad area of potential seagrass habitat encompassing 968 Ha between Wreck Island that separates South Bay from the Atlantic Ocean and the archipelago of marsh islands that define the western edge of South Bay (Fig. 7a). As before, the light blue shading represented intertidal areas shallower than 0 m (MLW) that we considered unsuitable for eelgrass colonization. Incorporating the epiphyte load used for Goodwin Islands reduced eelgrass density by 40% and the depth distribution by 35% relative to the epi-

phyte free simulation (Table 8; Fig. 5c vs. 5d), causing a southward contraction of the meadow away from Ship Shoal Inlet into shallower water and a corresponding reduction in shoot density in the deeper (mostly north) regions of the meadow (Fig. 7a vs. 7b). However, the depth distribution of eelgrass still extended to 1.1 m, 22% deeper than the limit for epiphyte-covered eelgrass at Goodwin Islands. Warm water temperature (30°C) had a minor effect on the depth distribution of epiphyte-free eelgrass, and reduced the maximum sustainable shoot density 16% relative to the cool simulation (Table 8; Fig. 5c). The warming-induced reduction in sustainable shoot density thinned the meadow along the eastern edge of Man and Boy Marsh (Fig. 7a vs.7c) but the effect was less dramatic than for Goodwin Islands. Epiphytes and warm water combined to reduce the depth distribution to 0.9 m and the maximum sustainable LAI to 4.7, relative to the cool water simulation with epiphytes, resulting in a general contraction of eelgrass in both the northern and

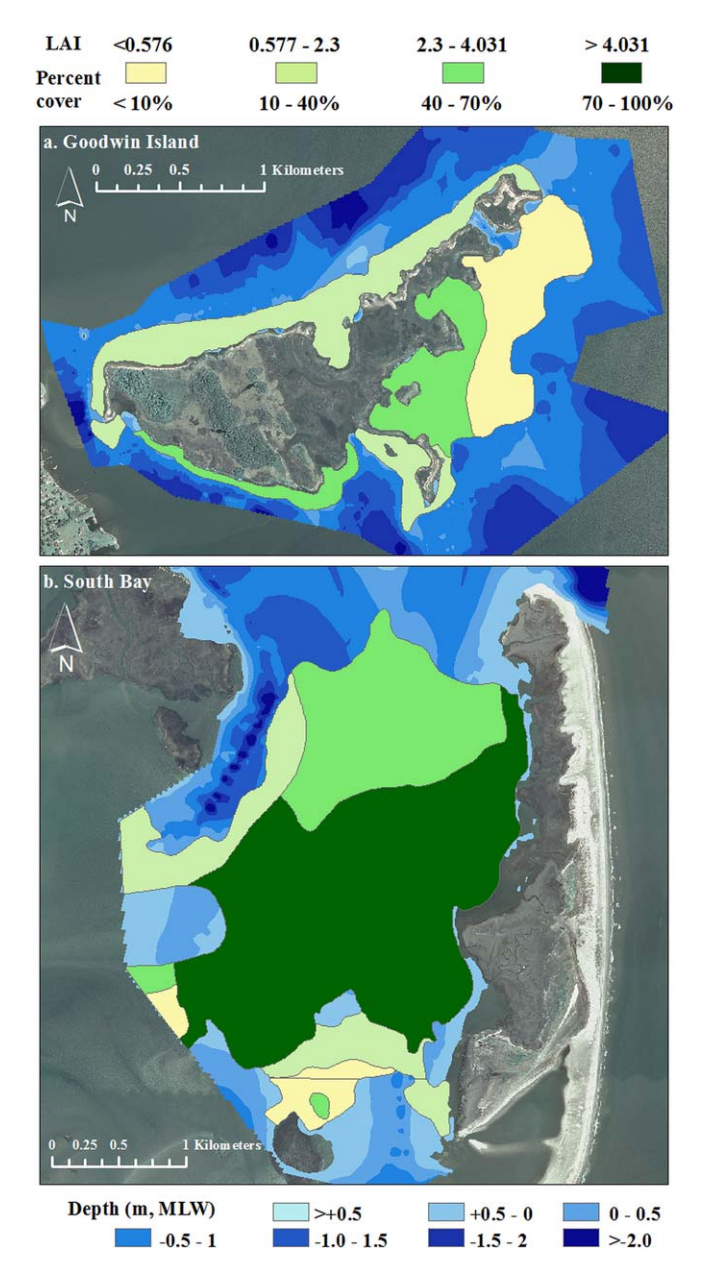


Fig. 8. 2011 maps of SAV distribution (eelgrass + widgeongrass) (tan to green colors) generated by the Virginia Institute of Marine Science SAV program (hppt://web.vims.edu/bio/sav/) for (a) Goodwin Islands and (b) South Bay overlain on DEMs (blue colors) generated by our bathymetric surveys. [Color figure can be viewed in the online issue, which is available at wileyonlinelibrary.com.]

southern regions of South Bay, and a general thinning of the entire meadow (Table 8; Figs. 5d, 7d). Raising the pCO_2 to a mid-century level of 600 μ Atm nearly compensated for the negative effects of thermal stress both in the absence and presence of epiphytes, virtually restoring densities and depth distributions to those of the cool water simulations (Table 8; Fig. 7e,f). The end-of-century pCO_2 simulation (870 μ Atm) under warm summer conditions increased the sustainable density beyond the cool water simulations by 4% without

epiphytes and by 2% with epiphytes, but did not substantially increase the depth distribution (Table 8; Figs. 5c,d, 7g,h). In all simulations, the central region of South Bay was remarkably unaffected by warm water, the presence of epiphytes or increasing CO_2 , suggesting that the average water quality of this coastal lagoon provides a more robust environment for eelgrass than Goodwin Islands.

Validating model predictions against in situ observations

Although the impacts of future climate change on eelgrass distribution projected for these sites cannot be validated in an absolute sense, we can assess the ability of GrassLight to predict existing eelgrass distributions at these sites. Model predictions of eelgrass presence or absence from the Cool 2011 simulation with epiphytes showed a high degree of fidelity to the 2011 maps generated by the VIMS SAV project for Goodwin Islands (Fig. 6b vs. 8a). Of the 43,501 pixels scored for the Goodwin Islands site where depths were 2.0 m or shallower, there was 99% agreement in terms of eelgrass presence and 63% agreement in terms of eelgrass absence (Table 9a). However, the model predicted slightly more vegetated pixels than indicated on the VIMS SAV map (11,228 vs. 11,191). Of the 11,228 pixels determined to be vegetated by both GrassLight and the VIMS SAV map, densities predicted by GrassLight were consistent with VIMS assignments 18% of the time (diagonal sum = 1995 pixels, Table 9b). The greatest discrepancy between modeled and measured densities occurred with the lowest density (Class 1), to which 4752 pixels were assigned by the VIMS map. In contrast GrassLight predicted only 111 pixels (2%) in Density Class 1, with most of the remaining pixels assigned to Density Classes 2 and 3 (Table 9b). Density Class 2 showed better agreement (25%) between model predictions and the measured polygons, with most of the disagreement resulting from model assignments to Class 3. Class 3 comparisons revealed the best level of agreement (40%) between GrassLight predictions and VIMS observations, with most of the error resulting from model assignment of these pixels to Density Class 4. GrassLight assigned 25% of the vegetated pixels in shallow water to density Class 4, but none were assigned to this highest density class by the VIMS analysis.

GrassLight predictions of eelgrass distribution at South Bay for the Cool 2011 climate (without epiphytes) included all 38,508 vegetated pixels derived from the VIMS SAV map (Table 10a), and generated a similar spatial pattern of distribution (Fig. 7a vs. 8b). Of the 38,508 pixels determined to be vegetated by both the model and the VIMS SAV maps, densities were consistent with VIMS assignments 54% of the time (diagonal sum = 20,944 out of 38,508 pixels, Table 10b). The greatest agreement between modeled and measured densities occurred with Density Classes 1 and 4, to which 0 and 20,505 pixels, respectively, were assigned by both the model and the VIMS SAV polygons. The model assigned 130 pixels to Density Class 2, compared to the

Table 9. Error matrices comparing model predictions of **a. Eelgrass presence/absence** and **b. Abundance** for the Cool 2011 simulation (including epiphytes) against density classes determined from aerial photography by the VIMS SAV project for the Goodwin Islands, VA. Values indicate the number of pixels for each category, with percentages of column totals in parentheses.

a. Presence/Absence		Measured	Measured	
Modeled	Present	Absent	Row Sum	
Present	11,228 (99%)	12,430 (37%)	23,658	
Absent	75 (1%)	22,254 (63%)	21,329	
Column Sum	11,303	33,684	44,987	

b. Abundance Modeled Density	Measured density				
	Class 1 <10% Cover	Class 2 10–40% Cover	Class 3 40–70% Cover	Class 4 >70% Cover	Row Sum
Class 1	111 (2%)	103 (2%)	25 (1%)	0	239
Class 2	1766 (37%)	1106 (25%)	369 (19%)	0	3241
Class 3	2159 (45%)	2024 (45%)	778 (40%)	0	4961
Class 4	716(15%)	1277 (28%)	794 (40%)	0	2787
Column Sum	4752	4510	1966	0	11228

Table 10. Error matrices comparing model predictions of **a. Eelgrass presence/absence** and **b. Abundance** for the Cool 2011 simulation (no epiphytes) against density classes determined by the VIMS SAV project from human interpretation of aerial photography for South Bay, Virginia, U.S.A. Values indicate the number of pixels for each category, with percentages of column totals in parentheses.

a. Presence/Absence		Measured	
Modeled	Present	Absent	Row Sum
Present	38,508 (99.9%)	58,186 (88%)	96,694
Absent	48 (0.1%)	8102 (12%)	8150
Column Sum	38,556	66,288	104,844

b. Abundance Modeled Density		Measured density				
	Class 1 <10% Cover	Class 2 10–40% Cover	Class 3 40–70% Cover	Class 4 >70% Cover	Row Sum	
Class 1	0	0	0	0	0	
Class 2	0	21 (0.4%)	109 (1%)	0	130	
Class 3	0	325 (6.6%)	873 (7%)	0	1198	
Class 4	128	4737 (93%)	12,265 (93%)	20,050 (100%)	37,180	
Column Sum	128	5083	13,247	20,050	38,508	

VIMS assignment of 5038 and 1198 pixels to Density Class 3 compared to the VIMS assignment of 13,247.

Discussion

The modeling efforts presented here provide a predictive theoretical environment for evaluating the interactive effects of water quality, temperature, OA/OC, and epiphyte load on the eelgrass distribution that can be extremely difficult to observe in nature when all are changing simultaneously but with independent trajectories. Although the model structure presently ignores physiological acclimation to temperature (Winters et al. 2011; Franssen et al. 2012), it produced eelgrass distributions and densities similar to those observed at Goodwin Islands and South Bay in 2011, and showed different sensitivities to the effects of warm summer temperatures on eelgrass distributions at these sites that resulted from differences in light attenuation.

The mechanistic linkages between temperature, pCO_2 , water quality parameters and submerged plant canopy

architecture provided by this radiative transfer approach extend our predictive ability beyond survival depth limits (Dennison et al. 1993; Gallegos 2001; Kenworthy et al. 2014) to the mapping of shoot density across the submarine landscape as a function of light quality, as well as light quantity. The seagrass canopy portion of *GrassLight* was previously shown to accurately predict seagrass density and distribution in Elkhorn Slough, CA, Dumas Bay, WA, and Florida Bay, FL (Zimmerman 2006; McPherson et al. 2011). This formulation has also been used to quantify important derived properties, such as δ^{13} C composition, that varies inversely with $H_{\rm sat}$ and may serve as a useful indicator of light limitation and system-level productivity (Hu et al. 2012; McPherson et al. 2015).

Broadening the utility of this approach to other environments, particularly for resource management purposes, has been hindered by the need for reliable estimates of $K_d(\lambda)$. The efforts published previously relied on direct measures of $K_{\rm d}(\lambda)$ and/or values generated by the commercial radiative transfer model Hydrolight (Mobley 1989) that required explicit knowledge of spectral absorption $[a(\lambda)]$ and beam attenuation $[c(\lambda)]$ coefficients, as well as volume scattering functions that limited the utility of GrassLight for resource management purposes. The analysis presented here demonstrated that the semianalytical relationship of Lee et al. (2005) required very little adjustment for differences in IOPs to accurately estimate $K_d(\lambda)$ for the optically distinct environments of Goodwin Islands (Chl-dominated) and South Bay (sediment dominated) from routinely monitored values of [Chl a] and [TSM]. Further, the ability to predict spectral irradiances, and not just broadband PAR, provides a pathway for resolving the apparent differences in perceived light requirements of SAV growing in turbid vs. clear water (Duarte et al. 2007) that may result from differences in light quality as well as light quantity (Hu et al. 2012) or other environmental consequences of eutrophication (Krause-Jensen et al. 2011; Kenworthy et al. 2014).

Although the model was parameterized separately with respect to $b_{\rm bp}(555)/b_{\rm p}(555)$ for Goodwin Islands and South Bay, the 25% difference in the value of the backscattering ratio affected $K_d(\lambda)$ by < 10% and the eelgrass depth distribution by < 5% (simulations not shown), suggesting that a common parameterization of the backscattering ratio would not have adversely affected model accuracy. Using the parameterizations employed here, including $b_{\rm bp}(555)/$ $b_{\rm p}(555) = 0.016$, the model estimated the spatial distribution of $K_d(\lambda)$ throughout West Falmouth Harbor, MA with a mean RMS error of 0.07 m⁻¹using water quality estimates of CDOM absorption, [Chl a] and [TSM], but without specific knowledge of IOPs or their relations to water quality parameters (del Barrio et al. 2014). However, successful application of the model to these environments does not guarantee it will work in all instances, and some effort should be made to validate the relationships between IOPs and water quality measures when applying the model to new environments.

Water quality plays a well-documented role in controlling seagrass depth distributions, especially in the Chesapeake Bay. Although both sites were turbid ($b_{avg} = 6.8 \& 5.4 \text{ m}^{-1}$ for Goodwin Islands and South Bay, respectively) and experienced similar concentrations of TSM, the Goodwin Islands site was more eutrophic, as indicated by significantly higher concentrations of Chl a, while the waters of South Bay contained a higher mineral fraction, as indicated by the higher backscattering ratio (Snyder et al. 2008). However, inorganic suspended sediment contributes more to scattering than absorption, reducing its impact on light attenuation relative to phytoplankton Chl a, which competes directly for light with eelgrass. This led to higher light attenuation at Goodwin Islands, particularly in the photosynthetically preferred (blue) part of the spectrum. As a result, reduced transparency of the water column around Goodwin Islands reduced the density and depth distribution of light-limited eelgrass at Goodwin Islands relative to South Bay and rendered the Goodwin Islands population more vulnerable to thermal stress and epiphyte loading in a manner consistent with historical observations (Moore and Jarvis 2008; Orth et al. 2010).

The accurate simulation of eelgrass depth distribution and density across the submarine landscape for present-day conditions at Goodwin Islands and South Bay provides some confidence in the ability of GrassLight to predict the response of eelgrass to changing climatic conditions anticipated for the next century. Model estimates of eelgrass presence/ absence were generally consistent with field observations at both sites. Model predictions of eelgrass density agreed with field observations almost half the time, with most errors representing assignments to adjacent density classes. The reduced coherence between the modeled and measured density class relative to presence or absence resulted, at least in part, from differences in textural resolution between Grass-Light predictions that assigned each pixel a unique %Cover estimate based on its depth, and the observational matrix in which all pixels were assigned the same density within an expertly drawn polygon. Visual inspection of the VIMS images used to generate the polygons (available at http:// www.vims.edu/bio/sav) revealed a considerable degree of texture with regard to apparent shoot density and patchiness that were not captured by the polygons. Furthermore, it must be emphasized that the field observations represent snapshots of realized plant distributions that may not be in steady state with respect to the environmental parameters used to drive GrassLight predictions to light-limited densities. The Goodwin Islands population has been subjected to a number of stress events, most recently the extremely warm summer of 2010 (Moore et al. 2012), and its 2011 distribution probably was lower than the light-limited potential predicted by GrassLight. Additionally, the restored eelgrass

meadow in South Bay is still expanding outward from the original restoration effort that began in 2000 (Orth et al. 2006a).

The model calculations performed here suggest that epiphyte densities reported for Goodwin Islands eelgrass can reduce the potential density and depth distribution of eelgrass by about 50% relative to the epiphyte-free simulation, and their incorporation more accurately predicted eelgrass distribution and density relative to the field observations. For these simulations, the epiphyte effect was parameterized using the data of Bulthuis and Woelkerling (1983) that strongly attenuate light as a function of epiphyte density in a spectrally neutral manner. However, considerable variability exists in this relationship depending on the taxonomic and anatomic nature of the epiphytes (e.g., encrusting vs. upright filamentous) (Brush and Nixon 2002), the degree to which carbonate structures and sediment particles are incorporated into the leaf biofilm and spectral effects (Drake et al. 2003) not considered here. Although our calculations are consistent with other reports demonstrating the negative effects of epiphyte loads in the range of 1–3 mg DW cm⁻² on leaf photosynthesis (Sand-Jensen 1977; Sand-Jensen and Borum 1984; Cebrián et al. 1999) there is considerable room for improvement in modeling this relationship in response to particular environments. In addition to being stimulated by eutrophication (Moore 2004; Orth et al. 2006a), epiphyte densities are also affected by grazing intensity that can vary with seagrass density/distribution (van Montrfrans et al. 1984; Duffy 2006; Hughes et al. 2013). Thus, environmental stresses that cause periodic eelgrass die-backs, particularly at Goodwin Islands, may reduce the biodiversity and trophic structure of the animal community within the meadow, further promoting epiphyte growth and preventing eelgrass from occupying potential habitat based on water quality measures alone.

It must be emphasized that these GrassLight predictions represent steady-state densities based on clear sky light availability and metabolic carbon balance driven by photosynthesis and respiration. Consequently, they should be viewed as upper (optimistic) limits that do not presently account for other processes that may directly affect seagrass abundance, such as acute toxic effects of nutrients in the water column or porewater (Burkholder et al. 1992), porewater sulfide (Holmer et al. 2005; Govers et al. 2014), sediment grain size, organic matter content and wave exposure (Koch 2001; Infantes et al. 2009). Although used here to determine steady-state responses to constant environmental conditions, the formulations underlying GrassLight can be implemented to simulate the dynamic temporal response of eelgrass carbon balance to varying environmental conditions on time scales ranging from seconds to seasons and years (Zimmerman et al. 1994; Kraemer and Alberte 1995; Zimmerman et al. 2001). Unlike the open ocean, local metabolic processes can produce dramatic, high frequency variations in the pCO₂/pH status of estuarine waters that overwhelm the equilibrating dynamics of air-sea gas exchange driving anthropogenic OA (Duarte et al. 2013) and may be important in explaining the persistence, as well as the disappearance, of seagrasses in response to changes in the trophic status of estuarine ecosystems (Howarth et al. 2014). Further, summer heat stress may occur as a series of relatively short heat waves, lasting two to three weeks that exceed the average temperature differences used here (Bergmann et al. 2010; Winters et al. 2011). Finally, increased rates of photosynthesis derived from elevated [CO₂] will facilitate the summertime accumulation of carbon reserves in plants growing at depths shallower than the survival thresholds defined here, that enhance winter survival and flower production in the following spring (Palacios and Zimmerman 2007).

Although declining water quality has been repeatedly identified as an existential threat to seagrass communities worldwide, rising water temperature represents a particular concern for Chesapeake Bay eelgrass located near the southern limit of their distribution on the Atlantic coast of North America (Orth et al. 2010). When properly constrained and parameterized to accurately reproduce local conditions, the GrassLight model offers predictive insights into the performance of eelgrass meadows that can inform our understanding of ecosystem responses to future climate change. With respect to the Chesapeake region, our results suggest that OA/OC projected for the next century will stimulate photosynthesis sufficiently to offset the negative effects of temperature on eelgrass survival. Thus, continued efforts to improve water quality, particularly within the Chesapeake Bay, should facilitate the survival of eelgrass despite a warmer climate. Additionally, the reduced temperature sensitivity exhibited by South Bay populations in the simulations performed here suggests that improved water quality may reduce the effects of thermal stress on populations growing near their southern limits, even in the absence of CO₂-stimulated photosynthesis. These findings should provide further incentive to improve coastal water quality in support of SAV habitat restoration goals.

References

Batiuk, R., and others. 1992. Chesapeake bay submerged aquatic vegetation habitat requirements and restoration targets: A technical synthesis. U.S. Environmental Protection Agency.

Beer, S., and E. Koch. 1996. Photosynthesis of marine macroalgae and seagrasses in globally changing CO₂ environments. Mar. Ecol. Prog. Ser. **141**: 199–204. doi:10.3354/meps141199

Bergmann, N., and others 2010. Population-specificity of heat stress gene induction in northern and southern eelgrass *Zostera marina* populations under simulated global

- warming. Mol. Ecol. **19**: 2870–2883. doi:10.1111/j.1365-294X.2010.04731.x
- Biber, P., C. Gallegos, and J. Kenworthy. 2008. Calibration of a bio-optical model in the North River, NC: A tool to evaluate water quality impacts on seagrasses. Estuaries Coast. **31**: 177–191. doi:10.1007/s12237-007-9023-6
- Bowers, D., and C. Binding. 2006. The optical properties of mineral suspended particles: A review and synthesis. Estuar. Coast. Shelf Sci. **67**: 219–230. doi:10.1016/j.ecss.2005.11.010
- Bricaud, A., A. Morel, and L. Prieur. 1981. Absorption by dissolved organic matter of the sea (yellow substance) in the UV and visible domains. Limnol. Oceanogr. **26**: 43–53. doi:10.4319/lo.1981.26.1.0043
- Bricaud, A., M. Babin, A. Morel, and H. Claustre. 1995. Variability in the chlorophyll-specific absorption coefficients of natural phytoplankton: Analysis and parameterization. J. Geophys. Res. **100**: 13321–13332. doi:10.1029/95JC00463
- Brush, M., and S. Nixon. 2002. Direct measurements of light attenuation by epiphytes on eelgrass *Zostera marina*. Mar. Ecol. Prog. Ser. **238**: 73–79. doi:10.3354/meps238073
- Bulthuis, D., and W. Woelkerling. 1983. Biomass accumulation and shading effects of epiphytes on leaves of the seagrass, *Heterozostera tasmanica*, in Victoria, Australia. Aquat. Bot. **16**: 137–148. doi:10.1016/0304-3770(83)90089-X
- Burkholder, J. M., K. M. Mason, and H. B. Glasgow. 1992. Water-column nitrate enrichment promotes decline of eelgrass Zostera marina: Evidence from seasonal mesocosm experiments. Mar. Ecol. Prog. Ser. 81: 163–178. doi:10.3354/meps081163
- Cebrián, J., S. Enríquez, M. Fortes, N. Agawin, J. Vermaat, and C. Duarte. 1999. Epiphyte accrual on *Posidonia oceanica* (L.) Delile leaves: Implications for light absorption. Bot. Mar. **42**: 123–128. doi:10.1515/BOT.1999.015
- Cleveland, J., and A. Weidemann. 1993. Quantifying absorption by aquatic particles: A multiple scattering correction for glass-fiber filters. Limnol. Oceanogr. **38**: 1321–1327. doi:10.4319/lo.1993.38.6.1321
- Cummings, M., and R. Zimmerman. 2003. Light harvesting and the package effect in *Thalassia testudinum* Koenig and *Zostera marina* L.: Optical constraints on photoacclimation. Aquat. Bot. **75**: 261–274. doi:10.1016/S0304-3770(02)00180-8
- del Barrio, P., N. K. Ganju, A. L. Aretxabaleta, M. Hayn, A. García, and R. W. Howarth. 2014. Modeling future scenarios of light attenuation and potential seagrass success in a eutrophic estuary. Estuar. Coast. Shelf Sci. **149**: 13–23. doi:10.1016/j.ecss.2014.07.005
- Dennison, W., and others 1993. Assessing water quality with submersed aquatic vegetation. BioScience **43**: 86–94. doi: 10.2307/1311969
- Drake, L., F. Dobbs, and R. Zimmerman. 2003. Effects of epiphyte load on optical properties and photosynthetic potential of the seagrasses *Thalassia testudinum* Koenig and *Zostera marina* L. Limnol. Oceanogr. **48**: 456–463. doi:10.4319/lo.2003.48.1 part 2.0456

- Duarte, C. 1991. Seagrass depth limits. Aquat. Bot. **40**: 363–377. doi:10.1016/0304-3770(91)90081-F
- Duarte, C., N. Marbà, D. Krause-Jensen, and Sánchez-Camacho. 2007. Testing the predictive power of seagrass depth limit models. Estuaries Coast. **30**: 652–656. doi: 10.1007/BF02841962
- Duarte, C., and others 2013. Is ocean acidification an openocean syndrome? Understanding the drivers and impacts of pH variability in coastal ecosystems. Estuaries Coast. **36**: 221–236. doi:10.1007/s12237-013-9594-3
- Duffy, J. 2006. Biodiversity and the functioning of seagrass ecosystems. Mar. Ecol. Prog. Ser. **311**: 233–250. doi: 10.3354/meps311233
- Evans, A. S., K. L. Webb, and P. A. Penhale. 1986. Photosynthetic temperature acclimation in two coexisting seagrasses, *Zostera marina* L. and *Ruppia maritima* L. Aquat. Bot. **24**: 185–197. doi:10.1016/0304-3770(86)90095-1
- Fabry, V., B. Seibel, R. Feely, and J. Orr. 2008. Impacts of ocean acidification on marine fauna and ecosystem processes. ICES J. Mar. Sci. **65**: 414–432. doi:10.1093/icesjms/fsn048
- Falkowski, P., and J. Raven. 2007. Aquatic photosynthesis, 2nd ed. Princeton.
- Franssen, S., and others. 2012. Transcriptomic resilience to global warming in the seagrass *Zostera marina*, a marine foundation species. Proc. Natl. Acad. Sci. USA **108**: 19276–19281. doi:10.1073/pnas.1107680108
- Gallegos, C. 1994. Refining habitat requirements of submersed aquatic vegetation: Role of optical models. Estuaries **17**: 187–199. doi:10.2307/1352568
- Gallegos, C. 2001. Calculating optical water quality targets to restore and protect submersed aquatic vegetation: Overcoming problems in partitioning the diffuse attenuation coefficient for photosynthetically active radiation. Estuaries **24**: 381–397. doi:10.2307/1353240
- Gallegos, C., and P. Neale. 2002. Partitioninf of spectral absorption in Case 2 waters: Discrimination of dissolved and particular components. Appl. Opt. **41**: 4220–4233. doi:10.1364/AO.41.004220
- Govers, L., and others 2014. Toxic effects of increased sediment nutrient and organic matter loading on the seagrass *Zostera noltii*. Aquat. Toxicol. **155**: 253–260. doi:10.1016/j.aquatox.2014.07.005
- Gregg, W., and K. Carder. 1990. A simple spectral solar irradiance model for cloudless maritime atmospheres. Limnol. Oceanogr. **35**: 1657–1675. doi:10.4319/lo.1990.35.8. 1657
- Holmer, M., M. Frederiksen, and H. Møllegaard. 2005. Sulfur accumulation in eelgrass (Zostera marina) and effect of sulfur on eelgrass growth. Aquat. Bot. **81**: 367–379. doi: 10.1016/j.aquabot.2004.12.006
- Howarth, R., and others 2014. Metabolism of a nitrogenenriched coastal marine lagoon during the summertime. Biogeochemistry **118**: 1–20. doi:10.1007/s10533-013-9901-x

- Hu, X., D. Burdige, and R. Zimmerman. 2012. δ^{13} C is a signature of light availability and photosynthesis in seagrass. Limnol. Oceanogr. **57**: 441–448. doi:10.4319/lo.2012.57.2.0441
- Hughes, B., and others 2013. Recovery of a top predator mediates negative eutrophic effects on seagrass. Proc. Natl. Acad. Sci. USA **110**: 15313–15318. doi:10.1073/pnas. 1302805110
- Infantes, E., J. Terrados, A. Orfila, B. Cañellas, and A. Álvarez-Ellacuaria. 2009. Wave energy and the upper depth limit distribution of *Posidonia oceanica*. Botanica Marina **52**: 419–427. doi: 10.1515/BOT.2009.050
- Invers, O., R. Zimmerman, R. Alberte, M. Perez, and J. Romero. 2001. Inorganic carbon sources for seagrass photosynthesis: An experimental evaluation for bicarbonate use in temperate species. J. Exp. Mar. Biol. Ecol. **265**: 203–217. doi:10.1016/S0022-0981(01)00332-X
- IPCC. 2013. Climate change 2013: The physical science basis, p. 1535. In T. Stocker et al [eds.], Contribution of working group I to the fifth assessment report of the intergovernmental panel on climate change. Cambridge, UK.
- Jeffrey, S. W., and G. F. Humphrey. 1975. New spectrophotometric equations for the determination of chlorophylls a, b, c1 and c2 in higher plants, algae and natural phytoplankton. Biochem. Physiol. Pflanz. **167**: 191–194.
- Kenworthy, J., C. Gallegos, C. Costello, D. Field, and G. di Carlo. 2014. Dependence of eelgrass (Zostera marina) light requirements on sediment organic matter in Massachusetts coastal bays: Implications for remediation and restoration. Mar. Pollut. Bull. 83: 446–157. doi:10.1016/j.marpolbul. 2013.11.006
- Koch, E. 2001. Beyond light: Physical, geological and geochemical parameters as possible submersed aquatic vegetation habitat requirements. Estuaries **24**: 1–17. doi:10.2307/1352808
- Kraemer, G. P., and R. S. Alberte. 1995. Impact of daily photosynthetic period on protein synthesis and carbohdyrate stores in Zostera marina L. (eelgrass) roots: Implications for survival in light limited environments. J. Exp. Mar. Biol. Ecol. 185: 191–202. doi:10.1016/0022-0981(94)00145-4
- Krause-Jensen, D., and others 2011. Sea bottom characteristics affect depth limits of eelgrass *Zostera marina*. Mar. Ecol. Prog. Ser. **425**: 91–102. doi:10.3354/meps09026
- Lee, Z.-P., K. Du, and R. Arnone. 2005. A model for the diffuse attenuation coeffficient of downwelling irradiance. J. Geophys. Res **110: 1–10.** doi:10.1029/2004JC002275
- Lee, Z., A. Weidemann, J. Kindle, R. Arnone, K. Carder, and C. Davis. 2007. Euphotic zone depth: Its derivation and implication to ocean color remote sensing. J. Geophys. Res **112**: C03009. doi:10.1029/2006JC003802
- Lewis, E., and D. Wallace. 1998. Program developed for CO₂ system calculations, p. 18. ORNL/CDIAC-105.
- Maffione, R., and D. Dana. 1997. Instruments and methods for measuring the backward-scattering coefficient of ocean waters. Appl. Opt. **26**: 6058–6067. doi:10.1364/AO.36.006057

- Magnusen, A., L. Harding, M. Mallonee, and J. Adolf. 2004. Bio-optical model for the Chesapeake Bay and the Middle Atlantic Bight. Estuar. Coast Shelf Sci. **61**: 403–424.
- McPherson, M., V. Hill, R. Zimmerman, and H. Dierssen. 2011. The optical properties of Greater Florida Bay: Implications for seagrass abundance. Estuaries Coast. **34**: 1150–1160. doi:10.1007/s12237-011-9411-9
- McPherson, M., R. Zimmerman, and V. Hill. 2015. Environmental and physiological influences on productivity and carbon isotope discrimination in eelgrass (*Zostera marina* L.). Limnol. Oceanogr. **In Press**.
- Mitchell, B., M. Kahru, J. Wieland, M. Stramska, J. Mueller, and G. Fargion. 2002. Determination of spectral absorption coefficients of particles, dissolved material and phytoplankton for discrete water samples., p. 231–257. *In* J. Mueller and G. Farigon [eds.], Ocean Optics Protocols for Satellite Ocean Color Sensor Validation, Revision 3, V. 2. NASA.
- Mobley, C. 1989. A numerical model for the computation of radiance distribution in natural waters with windroughened surfaces. Limnol. Oceanogr. **34**: 1473–1483. doi:10.4319/lo.1989.34.8.1473
- Moore, K. 2004. The influence of seagrasses on water quality in shallow regions of the lower Chesapeake Bay. J. Coast. Res. **SI(45)**: 162–178. doi:10.2112/SI45-162.1
- Moore, K., and J. Jarvis. 2008. Environmental factors affecting summertime eelgrass diebacks in the lower Chesapeake Bay: Implications for long-term persistence J. Coast. Res. **55**: 135–147. doi:10.2112/SI55-014
- Moore, K., E. Shields, D. Parrish, and R. Orth. 2012. Eelgrass survival in two contrasting systems: Role of turbidity and summer water temperatures. Mar. Ecol. Prog. Ser. **448**: 247–258. doi:10.3354/meps09578
- Neckles, H. A., R. L. Wetzel, and R. J. Orth. 1993. Relative effects of nutrient enrichment and grazing on epiphytemacrophyte (Zostera marina L.) dynamics. Oecol. (Heidelberg) **36**: 265–274. doi:10.1007/BF00317683
- Neckles, H., E. Koepfler, L. Haas, R. Wetzel, and R. Orth. 1994. Dynamics of epiphytic photoautotrophs and heterotrophs in *Zostera marina* (eelgrass) microcosms: Responses to nutrient enrichment and grazing. Estuaries **17**: 597–605. doi:10.2307/1352407
- Nielsen, S., K. Sand-Jensen, J. Borum, and O. Geertz-Hansen. 2002. Depth colonization of eelgrass (*Zostera marina*) and macroalgae as determined by water transparency in Danish coastal waters. Estuaries **25**: 1025–1032. doi:10.1007/BF02691349
- Orth, R., M. Luckenback, S. Marion, K. Moore, and D. Wilcox. 2006a. Seagrass recovery in the Delmarva Coastal Bays, USA. Aquat. Bot. **84**: 26–36. doi:10.1016/j.aquabot.2005.07.007
- Orth, R., and others 2006b. A global crisis for seagrass ecosystems. BioScience **56**: 987–996. doi:10.1641/0006-3568(2006)56[987:AGCFSE]2.0.CO;2

- Orth, R., S. Marion, K. Moore, and D. Wilcox. 2010. Eelgrass (*Zostera marina* L.) in the Chesapeake Bay region of Mid-Atlantic coast of the USA: Challenges in conservation and restoration. Estuaries Coast. **33**: 139–150. doi:10.1007/s12237-009-9234-0
- Orth, R., D. Wilcox, J. Whiting, L. Nagey, A. Owens, and A. Kenne. 2012. Distribution of Submerged Aquatic Vegetation in the Chesapeake Bay and Coastal Bays 2011. VIMS Special Scientific Report Number 154. Final report to U.S. EPA Chesapeake Bay Program, Annapolis, MD. Grant No. CB963052-01-0. Available from http://www.vims.edu/bio/sav/sav11
- Palacios, S., and R. Zimmerman. 2007. Eelgrass (*Zostera marina* L.) response to CO₂ enrichment: Possible impacts of climate change and potential for remediation of coastal habitats. Mar. Ecol. Prog. Ser. **344**: 1–13. doi:10.3354/meps07084
- Pegau, W., R. Zaneveld, and J. Mueller. 2003. Volume absorption coefficients: Instruments, characterization, field measurements and data analysis protocols, p. 1–15. *In* J. Mueller and G. Fargion [eds.], Ocean optics protocols for satellite ocean color sensor validation Rev. 4. NASA.
- Pope, R., and E. Fry. 1997. Absorption spectrum (380-700 nm) of pure water. II. Integrating cavity measurements. Appl. Opt. **36**: 8710–8723. doi:10.1364/AO.36.008710
- Roesler, C., M. Perry, and K. Carder. 1989. Modeling in situ phytoplankton absorption from total absorption spectra in productive inland marine waters. Limnol. Oceanogr. **34**: 1510–1523. doi:10.4319/lo.1989.34.8.1510
- Sand-Jensen, K. 1977. Effect of epiphytes on eelgrass photosynthesis. Aquat.Bot. **3**: 55–63. doi:10.1016/0304-3770(77)90004-3
- Sand-Jensen, K., and J. Borum. 1984. Epiphyte shading and its effect on photosynthesis and diel metabolism of Lobelia dortmanna L. during the spring bloom in a danish lake. Aquat. Bot. **20**: 109–119. doi:10.1016/0304-3770(84)90031-7
- Shultis, J., and R. Myneni. 1988. Radiative transfer in vegetation canopies with anisotropic scattering. J. Quant. Spectrosc. Radiat. Transf. **39**: 115–129. doi:10.1016/0022-4073(88)90079-9
- Smith, R. D. 1989. Anaerobic metabolism in roots of the seagrass *Zostera marina*. The Univ. of Chicago.
- Smith, R. D., R. C. Zimmerman, and R. S. Alberte. 1988. Effects of long term anaerobiosis on carbon metabolism and respiration in roots of *Zostera marina* L. Eos **68**: 1741. doi:10.1007/BF00392668
- Snyder, W., and others 2008. Optical scattering and backscattering by organic and inorganic particulates in U.S. coastal waters. Appl. Opt. **47**: 666–677. doi:10.1364/ AO.47.000666
- Thayer, G., D. Wolfe, and R. Williams. 1975. The impact of man on seagrass systems. Am. Sci. **63**: 288–296.
- Tzortziou, M., and others. 2006. Bio-optics of the Chesapeake Bay from measurements and radiative transfer closure. Est. Coastal Shelf Sci. **68**: 348–362. doi:10.1016/j.ecss.2006.02.016

- van Montrfrans, J., R. Wetzel, and R. Orth. 1984. Epiphytegrazer relationships in seagrass meadows: Consequences for seagrass growth and production. Estuaries **7**: 289–309. doi:10.2307/1351615
- Wazniak, C., M. Hall, T. Carruthers, B. Sturgis, W. Dennison, and R. Orth. 2007. Linking water quality to living resources in a mid-Atlantic lagoon system. Ecol. Appl. **17**: S64–S78. doi:10.1890/05-1554.1
- Winters, G., P. Nelle, B. Fricke, G. Rauch, and T. Reusch. 2011. Effects of a simulated heat wave on photophysiology and gene expression of high- and low-latitude populations of *Zostera marina*. Mar. Ecol. Prog. Ser. **435**: 83–95. doi:10.3354/meps09213
- Zimmerman, R. 2003a. Appendix M. Final Report. A biophysical model evaluation of eelgrass distribution and habitat potential in Dumas Bay, WA. *In* H. D. Berry, A. T. Sewell, S. Wyllie-Echeverria, B. R. Reeves, T. F. Mumford, J. R. Skalski, R. C. Zimmerman, and J. Archer [eds.], Puget sound submerged vegetation monitoring project: 2000 2003 monitoring report, p. 60 pp plus appendices. Near-shore Habitat Program. Washington State Department of Resources.
- Zimmerman, R. 2003b. A biooptical model of irradiance distribution and photosynthesis in seagrass canopies. Limnol. Oceanogr. **48**: 568–585. doi:10.4319/lo.2003.48.1_part_2.0568
- Zimmerman, R. 2006. Chapter 13. Light and photosynthesis in seagrass meadows, p. 303–321. *In* A. Larkum, R. Orth, and C. Duarte [eds.], Seagrasses: Biology, ecology and conservation. Springer.
- Zimmerman, R. C., R. D. Smith, and R. S. Alberte. 1989. Thermal acclimation and whole plant carbon balance in *Zostera marina* L. (eelgrass). J. Exp. Mar. Biol. Ecol. **130**: 93–109. doi:10.1016/0022-0981(89)90197-4
- Zimmerman, R., A. Cabello-Pasini, and R. Alberte. 1994. Modeling daily production of aquatic macrophytes from irradiance measurements: A comparative analysis. Mar. Ecol. Prog. Ser. **114**: 185–196. doi:10.3354/meps114185
- Zimmerman, R., D. Kohrs, D. Steller, and R. Alberte. 1997. Impacts of CO_2 -enrichment on productivity and light requirements of eelgrass. Plant Physiol. **115**: 599–607. doi: 10/1104/pp/115.2.599
- Zimmerman, R., D. Steller, D. Kohrs, and R. Alberte. 2001. Top-down impact through a bottom-up mechanism: In situ effects of limpet grazing on growth, light requirements and survival of Zostera marina L. (eelgrass). Mar. Ecol. Prog. Ser. 218: 127–140. doi:10.3354/meps218127

Acknowledgments

Many thanks to Meredith McPherson, Malee Jinuntuya, Billur Celebi and David Ruble for assistance with field observations, sample processing Zimmerman et al.

and data analysis. We are grateful to R. J. Orth and members of the SAV Program (http://www.vims.edu/bio/sav) at the Virginia Institute of Marine Science, College of William and Mary for generously sharing SAV maps and polygons used in this analysis. Mark Brush provided substantive comments and suggestions that greatly improved the quality of the manuscript. Permission to conduct research at the Goodwin Islands was provided by the Chesapeake Bay National Estuarine Research Reserve Program. Financial support for this research was provided by Virginia

Sea Grant/NOAA (Award NA10OAR4170085) and the National Science Foundation (Award OCE-1061823).

Submitted 19 February 2015 Revised 17 June 2015 Accepted 17 June 2015

Editor: Robert Howarth